



## Research article

# Nuclear pore complexes concentrate on Actin/LINC/Lamin nuclear lines in response to mechanical stress in a SUN1 dependent manner



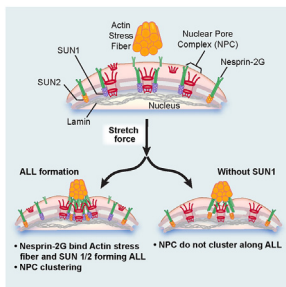
Mark A. Smith<sup>a,b,\*</sup>, Elizabeth Blankman<sup>a</sup>, Christopher C. Jensen<sup>a</sup>, Laura M. Hoffman<sup>a,b</sup>, Katharine S. Ullman<sup>a</sup>, Mary C. Beckerle<sup>a,b,c</sup>

<sup>a</sup> University of Utah Health Huntsman Cancer Institute, Salt Lake City, UT 84112, United States

<sup>b</sup> Department of Biology, Salt Lake City, UT 84112, United States

<sup>c</sup> Department of Oncological Sciences, University of Utah, Salt Lake City, UT 84112, United States

## GRAPHICAL ABSTRACT



## ARTICLE INFO

## Keywords:

LINC complex proteins  
Nuclear pore complex  
Mechanotransduction  
Actin stress fibers  
Actin/LINC/Lamin lines

## ABSTRACT

Formation of robust actomyosin stress fibers (SF) in response to cell stretch plays a key role in the transfer of information from the cytoplasm into the nucleus. Actin/LINC/Lamin (ALL) nuclear lines provide mechanical linkage between the actin cytoskeleton and the lamin nucleoskeleton across the nuclear envelope. To understand the establishment of ALL lines, we used live cell imaging of cells exposed to cyclic stretch. We discovered that nuclear pore complexes (NPCs) concentrate along ALL lines that are generated in response to uniaxial cyclic stretch. The ALL-associated NPCs display increased fluorescence intensity of nucleoporins Pom121, TPR and Nup153 relative to nucleoporins that are distal to the ALL lines. Here we test the hypothesis that a LINC complex component of ALL lines, SUN1 is involved in the integration of NPCs with ALL lines. We generated CRISPR SUN1 knockdown and knockout cell lines and show that SUN1 is essential for normal integration of NPCs to ALL lines. Loss or elimination of SUN1 significantly diminishes NPC/ALL line integration, demonstrating a key role for SUN1 in the recruitment or stabilization of NPCs to a discrete subdomain of the nuclear envelope at ALL lines. This work provides new insight into the mechanism by which cells respond to mechanical force through nuclear envelope remodeling.

\* Corresponding author.

E-mail address: [mark.smith@hci.utah.edu](mailto:mark.smith@hci.utah.edu) (M.A. Smith).

<https://doi.org/10.1016/j.heliyon.2022.e12147>

Received 3 September 2022; Received in revised form 14 November 2022; Accepted 29 November 2022

2405-8440/© 2022 The Author(s). Published by Elsevier Ltd. This is an open access article under the CC BY-NC-ND license (<http://creativecommons.org/licenses/by-nc-nd/4.0/>).

## 1. Introduction

Cells respond to mechanical force by transducing mechanical input into chemical signals. This is essential for the proper execution of processes in growth and development as well as tissue homeostasis. Mechanical force elicits characteristic cellular responses, including both morphological changes and biochemical signaling responses. However, the mechanisms and pathways by which mechanical signals are transduced into chemical responses are only beginning to be characterized. Within multicellular organisms, force input comes from varied sources, including stretch of tissues during locomotion or peristalsis (Ateshian and Humphrey, 2012), distension from changes in blood pressure (Deanfield et al., 2007), or from intracellular contraction or relaxation (Cramer et al., 1997), as well as from changes in axis orientation to execute migration processes (Fournier et al., 2010).

The cell is a mechanically integrated unit in which internal forces adjust to balance external forces and maintain mechanical homeostasis (Ingber, 1997). Transcellular mechanical connectivity has been demonstrated by experimentally pulling on integrins, transmembrane actin linked extracellular matrix receptors, which results in nuclear shape change as well as chromosome condensation changes (Maniotis et al., 1997a, 1997b). Other studies show mechanical stress drives nuclear accumulation of transcriptional coactivator Yes-associated protein (YAP) (Aragona et al., 2013; Dupont et al., 2011).

One striking morphological response of cells to mechanical force is the formation of actomyosin SFs (Byers et al., 1984; Wong et al., 1983). Recent studies have characterized the remodeling, reinforcement and repair response of the actin cytoskeleton to force changes (Roshanzadeh et al., 2020; Smith et al., 2010; Yoshigi et al., 2005). When cells are stretched along a single axis, SFs thicken and orient perpendicular to the axis of stretch (Yoshigi et al., 2005). While several different types of SFs have been described (Hotulainen and Lappalainen, 2006; Naumanen et al., 2008), we will concern ourselves here with dorsal SFs, which traverse above the nucleus. Dorsal SFs have clear roles in nuclear shape and positioning (Chang et al., 2015; Lombardi and Lammerding, 2011), and can be observed to exert downward pressure on the dorsal surface of the nucleus, thereby indenting it (Jorgens et al., 2016; Khatau et al., 2010; Li et al., 2014; Versaavel et al., 2014).

Furthermore, these structural changes trigger downstream nuclear responses. Work in our lab showed uniaxial cyclic stretch of cells grown on flexible membranes drives both YAP/TAZ and myocardin-related transcription factor (MRTF-A) to concentrate in the nucleus (Hoffman et al., 2020). This behavior may be explained, in part, by the observation that direct application of force to the nucleus through atomic force microscopy gates nuclear pores, promoting translocation of YAP into the nucleus (Elosegui-Artola et al., 2017). Consequently, it is essential to better understand the pathways and processes that coordinate the cytoplasmic and nuclear responses to mechanical cues.

The actin cytoskeleton connects structurally to the laminar nucleoskeleton via mechanically linked proteins embedded in the nuclear membrane. Referred to as the Linker of Nucleoskeleton and Cytoskeleton complex (LINC complex), these proteins enable force transfer between the cytoplasm and the nucleoplasm (Crisp et al., 2006; Starr, 2009; Starr and Fridolfsson, 2010). In the outer nuclear membrane are nesprins, of which nesprin-2Giant (N-2G) binds directly to cytoplasmic actin via a calponin homology domain at the end of a long chain of spectrin repeats (Mellad et al., 2011; Ostlund et al., 2009). N-2G has a conserved KASH domain in the nuclear intermembrane space, which interacts directly with the SUN (Sad1 and UNC84) domain of the SUN2 protein, which spans the inner nuclear membrane (Crisp et al., 2006).

N-2G and SUN2 concentrate along some SFs, which are closely associated with the nucleus (Luxton et al., 2010, 2011; Starr, 2010). With the N-2G attached to the actin SF, and SUN2 attached to both the N-2G and nucleoplasmic lamins, these structures couple the nucleus to dynamic, contractile actin SF, resulting in a nuclear-cytoplasmic connection essential for nuclear shape, polarization and positioning (Chang et al.,

2015; Hoffman et al., 2020; Lombardi and Lammerding, 2011; Luxton et al., 2011; Starr, 2010). N-2G and SUN2-rich regions of the nuclear envelope that align with actin SFs have been named Transmembrane Actin-associated Nuclear (TAN) lines. Our lab has shown in tissue culture population experiments that TAN lines form spontaneously in 14% of observed fields ( $n = 845$  nuclei). However, mechanical force effectively stimulates their formation. For example, exposure of cells to uniaxial cyclic stretch results in a four-fold increase, with 56% of fields showing TAN line formation (Hoffman et al., 2020).

We recently demonstrated that both lamin A/C and lamin B also are concentrated along these SF and associated LINC complex proteins tracts and that other nuclear surface proteins including SERCA2 and Sec61B do not (Hoffman et al., 2020). When viewed orthogonally, it is clear that with the actin SF sitting on the surface of the cell, SUN2 and laminA/C concentrate in the adjacent nuclear membrane. Work in endothelial cells plated on linearized extracellular matrix (Versaavel et al., 2014) raised concerns that this might be an imaging artifact due to the wrapping around of the nuclear membrane. However, that study, like ours, showed a significant concentration of LINC complex proteins along those tracts. Interestingly, we observe a similar concentration of LINC complex proteins in fibroblasts without any substantial indentation (Hoffman et al., 2020). The presence of significant concentrations of lamins is a finding that distinguishes the structures described herein from TAN lines. Therefore, we will refer to these structures as ALL nuclear lines, consistent with the molecular composition we observe. However, we would like to point out that the foundation of ALL (actin/LINC/Lamin) nuclear lines are TAN lines, with the basic TAN line components, an actin SF, the LINC complex proteins N-2G and SUN2 and the more recent addition of lamins, SUN1 and NPCs. Consequently, ALL lines are functionally identical to TAN lines in their formation in response to force and the fact that some SF in contact with the nuclear surface will form TAN or ALL lines and some will not. This study adds an important component to these structures in NPCs (Figure 1A).

NPCs are large, multi-protein complexes embedded in and spanning both leaflets of the nuclear membrane. NPCs are approximately 125 megaDaltons and 105 nm in diameter (Schuller et al., 2021), and are composed of approximately 30 different proteins assembled in eight-fold symmetry (Adams and Wente, 2013). NPCs are essential for regulating the flow of macromolecules both in and out of the nucleus. Our lab recently described the novel finding that with ALL line formation, NPCs also cluster along these tracts as evidenced by increased fluorescent signal of nucleoporins, such as Pom121 (Hoffman et al., 2020). This finding, as well as the demonstration that alterations in growth factor signaling by YAP and MRTF are similarly force responsive (Elosegui-Artola et al., 2017; Hoffman et al., 2020) raises important questions regarding force dependent clustering of NPCs along ALL lines which we will attempt to answer with this study.

In this work, we use live cell imaging to visualize and quantitate formation of ALL lines, characterizing their dynamic assembly properties. We show that when NPCs align and concentrate along ALL lines, they cluster and clump, as is demonstrated by the uniformly increased fluorescent intensity when detecting different nucleoporins. Using CRISPR-targeted SUN1 knockdowns and knockouts, we show SUN1 plays a key role in the localization of NPCs to ALL lines. This study expands upon the observation that NPCs accumulate along ALL nuclear lines to look at behavior of other nucleoporins, alterations in the structure of NPCs, recruitment dynamics of NPCs and potential anchoring proteins for NPCs to ALL lines.

## 2. Results

### 2.1. Mechanical force induces linear ALL lines that traverse the dorsal nuclear surface

Formation of ALL lines on the dorsal surface of nuclei occurs spontaneously in migrating adherent fibroblasts. ALL line formation can also be induced experimentally through stretching of the underlying

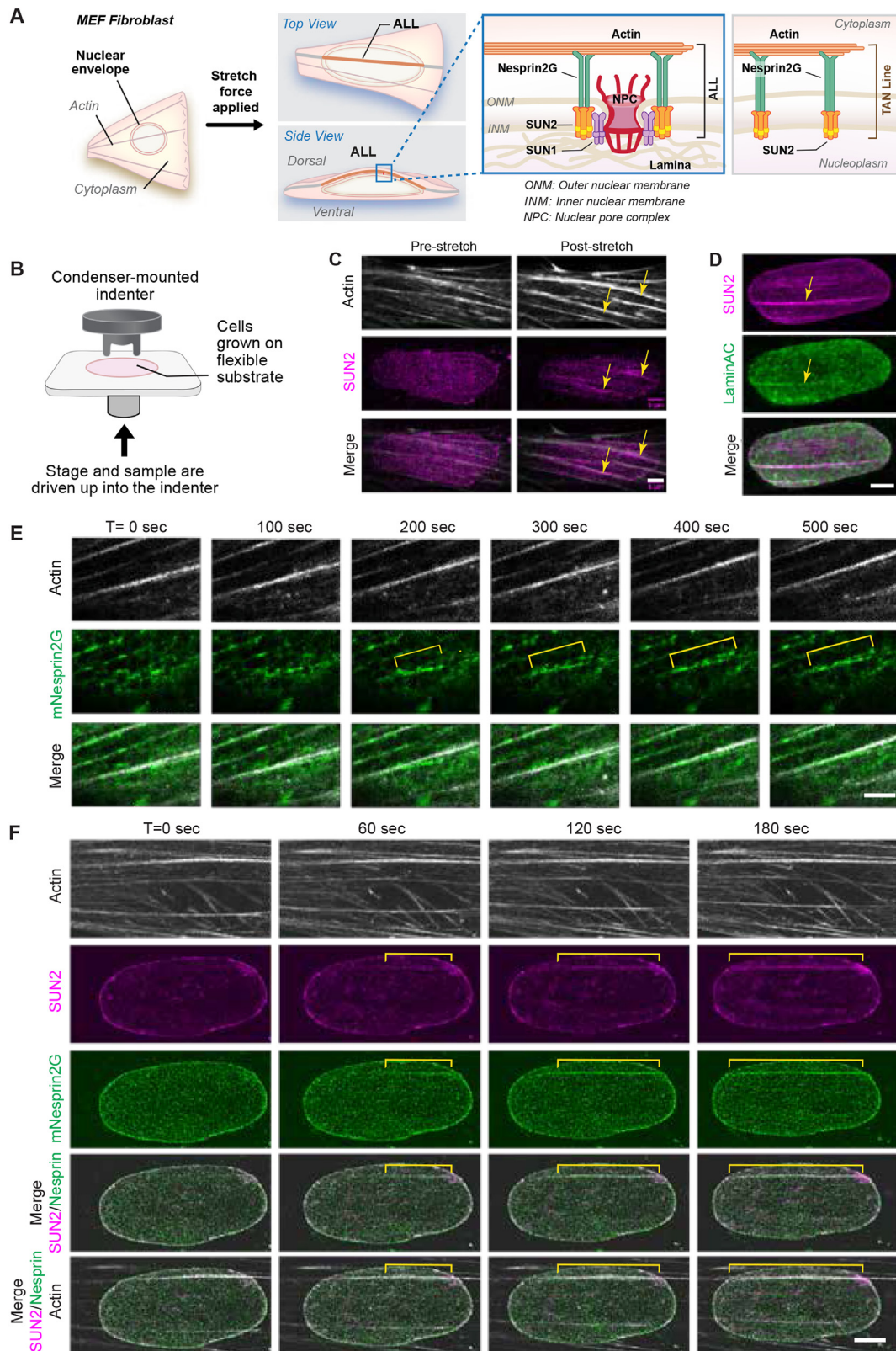


**Figure 1.** Stretch stimulated cells form actin/LINC/Lamin arrays that traverse the nuclear surface, mechanically linking the actin cytoskeleton to the nucleus. Nuclear pore complexes concentrate in a region flanking these structures. All scale bars are 5µm. A. Model shows cellular response to stretch via formation of ALL nuclear lines. Like TAN lines, ALL lines incorporate LINC complex proteins crossing the nuclear membrane. ALL nuclear lines additionally exhibit concentrated SUN1, nuclear lamins and NPCs. B. A system for stretching and imaging single cells. A condenser-mounted indenter above cells grown on flexible silicone membranes stretches the surface of the membrane and cell when cells and substrate are driven up via a piezo-controlled stage. C. LINC complex protein SUN2 concentrates along preexisting actin stress fibers in response to whole cell stretch. Yellow arrows show newly formed linear SUN2 accumulations. D. Lamin concentrates with LINC complex protein SUN2 at ALL lines. Yellow arrow shows ALL line. E. LINC complex protein mN-2G progressively assembles on preexisting actin SFs. Yellow brackets show accumulation of mN2G in a line. F. LINC complex proteins SUN2 and N-2G assemble concurrently and progressively on nuclear lines.

extracellular substrate (Figure 1A). The work described here utilizes multiple approaches for inducing and monitoring ALL line formation and dynamics and seeks to identify fundamental requirements for ALL line assembly.

To capture live cell events with appropriate temporal resolution, we innovated a system for stretching individual cells attached to silicone substrates (Figure 1B). In this system, cells are grown on silicone substrates that have extracellular matrix coupled to the surface to facilitate cell adhesion. These substrates contain sub-optical resolution fluorescent beads embedded in the surface providing fiducial marks that enable quantitation of the stretch magnitude. The substrate and cells are placed on the stage of an inverted microscope with a condenser-mounted indenter immediately above the cell to be stretched. The contact end of the indenter is either circular, for isotropic stretch, or has two prongs, for uniaxial stretch. The indenter dimensions are sufficient to flank a cell of interest that would be subjected to stretch. The sample (coverslip, silicone pad and cell) is raised, a precise amount, via a piezo controlled micropositioning stage, into the indenter. This stretches the substrate under the cell, resulting in a controlled stretch of the substrate-adherent cell (Rosner et al., 2017). This approach allows the real-time monitoring of protein dynamics during stretch, enabling visualization of protein enrichment along actin SFs in response to graded force inputs on various time scales.

Upon exposure to 15 min of indenter-mediated cyclic stretch stimulation, we observe the accumulation of LINC complex proteins such as SUN2 directly overlapping actin SFs (Figure 1C). Additionally, following a 60 min period of uniaxial cyclic stretch and sample fixation, we observe 36% of stress fibers that overlay nuclei have accumulated enriched levels of SUN2 ( $n = 76$  nuclei), while the other 74% of actin stress fibers that overlay nuclei do not accumulate SUN2 ( $n = 310$  nuclei). In addition to the SUN2 that accumulates along some of the actin SF, we also consistently observe the co-distribution of laminA/C (Figure 1D), the third component of the ALL line, whenever SUN2 is present. It remains unclear why some stress fibers contacting nuclei become ALL lines and some do not.

Live cell imaging of stretch-stimulated cells provides insight into the dynamic formation of ALL lines. Using a transiently transfected N-2G construct with a truncated second spectrin-like repeat called EGFP-mini-spectrin-2G (EGFP-mN-2G) (Luxton et al., 2010; Ostlund et al., 2009), we observe that EGFP-mN2G is dispersed on the surface of the nucleus in a largely homogeneous pattern with some nascent linear elements prior to stretch stimulation (Figure 1E, F;  $T = 0$  s). Upon exposure of the cell to cyclic uniaxial stretch at 10 s intervals, the mN2G-GFP is observed to integrate in alignment with cytoplasmic actin SFs that are closely apposed to the surface of the nucleus (Figure 1E). Stretch stimulation is thus observed to promote the co-localization of cytoplasmic actin SFs and N-2G associated with the nuclear envelope. In tandem with the stretch-dependent concentration of EGFP-mN-2G along the track of the actin SF (Figure 1F), SUN2 also accumulates coincident with EGFP-mN-2G (Figure 1F). These results illustrate that the formation of ALL lines is promoted in response to cell stretch, with accumulation of the LINC complex proteins, N-2G and SUN2, as well as laminA/C along sites of SF contact with the dorsal nuclear surface. The accumulation of N-2G follows the formation of actin SFs, with SUN2 accumulating simultaneously with the N-2G.

## 2.2. NPCs accumulate near ALL lines

NPCs are key components embedded in the nuclear envelope, and formation of ALL lines, either as the result of stretch or through spontaneous occurrence is accompanied by a substantial increase in the fluorescent signal of nucleoporins near ALL lines (Hoffman et al., 2020).

To better understand the nature of this observation, we needed a reproducible means of inducing and quantifying NPC response to stretch. We grew cells on flexible silicone substrates and subjected them to 1 h of uniaxial cyclic stretch, then fixed, antibody labeled, and imaged on the membranes using laser scanning confocal microscopy. ALL lines were

labeled using phalloidin staining of actin (Figure 2A–D) and indirect immunofluorescent labeling of laminA/C (Figure 2A and 2B) or SUN2 (Figure 2D). NPCs were labeled with antibodies specific for the NPC basket protein TPR (Figure 2A and B). The concentration of NPCs generally was generally detected in a region that is approximately 1  $\mu\text{m}$  wide, or 0.5  $\mu\text{m}$  on either side of the ALL lines central actin SF. Fluorescent intensity was measured for graphing using a 10-pixel (0.3  $\mu\text{m}$ ) wide linescan perpendicular to the ALL line. This shows the increase in fluorescent intensity in the region flanking the central actin SF (Figure 2A'). Unlike the laminA/C signal that directly overlays the actin signal, the fluorescent signals for the NPCs are dispersed in the  $\sim 1$   $\mu\text{m}$  wide region overlapping the actin SF. In some cases, the NPCs align on either side of the ALL line, creating the appearance of railroad tracks (Figure 2B and B').

It is striking that while some of the actin SFs in contact with the surface of the nucleus will form ALL lines and clustered NPCs, not all SFs do, for example as indicated by the yellow arrows in Figure 2A, B and C. As seen in Figure 2A', the actin SF that is engaged in an ALL line is also not necessarily the most robust SF with the strongest actin fluorescence intensity, which is marked with a yellow bracket and lacks colocalization of laminA/C and TPR. As with SUN2, 74% of the dorsal stress fibers overlaying the nuclei do not form ALL lines. We do not observe laminA/C, LINC complex proteins or NPCs aligning in the absence of actin SFs, thus the nuclear association of actin SFs is necessary, but not sufficient, for the recruitment of LINC complex proteins and laminA/C into linear elements on the nuclear envelope.

To rule out the possibility that we were observing the accumulation of an individual constituent of NPC, but not structurally mature NPCs, we immunolabeled with antibodies directed at other NPC constituents. As with the TPR labeling, with Pom121 immunolocalization, we see a concentration of NPCs near the ALL line (Figure 2C and 2C'). Additionally, clustering of NPCs proximal to ALL lines is observed when the cell is labeled with the antibody FG414 (Figure 2D and 2D'), which detects Nup62, Nup153 and other FG-repeat containing nucleoporins. Collectively, these findings support the view that we are imaging intact NPCs, not unassembled core constituents of the pores. These results are expanded upon and quantitated in Figures 6 and 7.

Using multiple labels and labeling approaches, the data presented here show that NPCs cluster and concentrate in the  $\sim 1$   $\mu\text{m}$  region flanking an ALL. Additionally, we have shown not all actin SFs that traverse the dorsal side of the nucleus produce ALLs or cluster NPCs. These data raise a few interesting questions. The first we would like to address is, are the increases in nucleoporin intensity detected proximal to the ALL line due to the individual pores being brighter, or to nuclear pores being more concentrated at this site?

## 2.3. Individual NPCs clustered proximal to ALL lines are fluorescently brighter than those that are distal

To determine whether the individual NPCs in the ALL-proximal region, 0.5  $\mu\text{m}$  on either lateral side, were brighter than those outside this region, we applied a software-based approach to identify ALL line as surface modeled 'Filaments' using a MATLAB plugin program in Imaris (Bitplane) that detects linear elements in three dimensions. We used another MATLAB plugin program in Imaris that identifies punctate 200 nm image elements in three dimensions as 'Spots' and finds their centers. We then binned the NPCs/Spots as either Near ( $<0.5$   $\mu\text{m}$ ) or Far ( $>0.5$   $\mu\text{m}$ ) based on location relative to the ALL/Filament. This enabled us to measure the mean fluorescent intensity of individual NPCs in either the near NPC group or the Far NPC group (Figure 3A).

Using the above approach and looking at the two groups of NPCs within single cells, we were able to compare the populations using pairwise T-tests (Figure 3B). This showed a robust and reproducible increase in fluorescent intensity in the proximal Spots/NPCs as opposed to the distal Spots/NPCs. This allowed us to determine that the discrete Spots/NPCs that are proximal to the ALL line are indeed individually brighter than those that are dispersed on the surface of the nucleus.

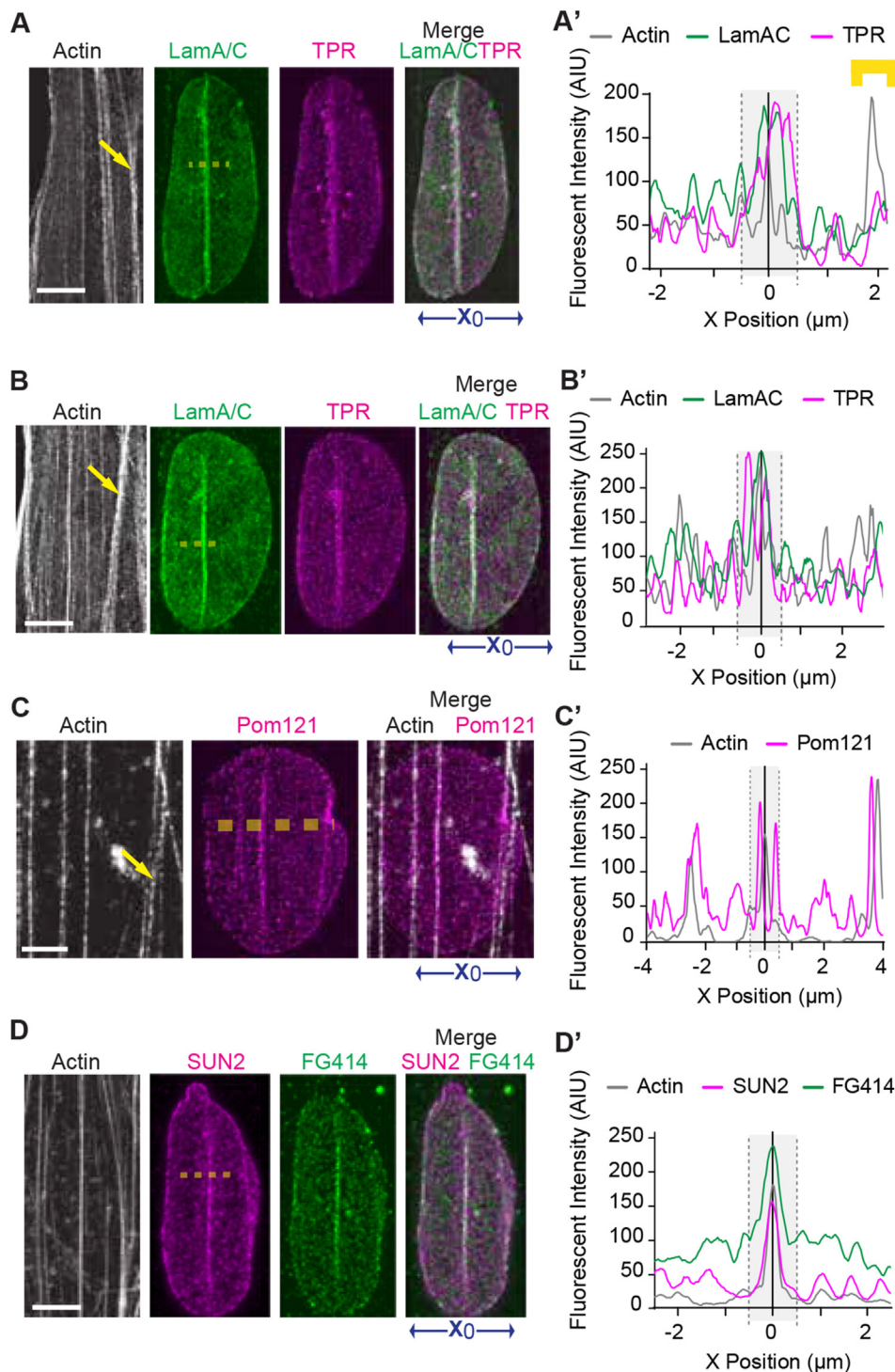


**Figure 2.** NPCs accumulate on ALL nuclear lines in an approximately  $1\mu\text{m}$  wide region flanking the ALL lines, and are brighter fluorescently along ALL lines. Cells were subjected to cyclic stretch, then fixed and antibody labeled. 10 pixel wide linescans for fluorescent intensity are measured along the yellow bar. Scale bars are all  $5\mu\text{m}$ . Grayed regions on the graphs show the  $1\mu\text{m}$  wide region flanking the ALL line. Yellow arrows show overlaid SF that do not form ALL lines. **A.** Actin and LaminA/C align on the dorsal surface of the nucleus. Nucleoporin TPR shows accumulation of NPC flanking the actin and LaminA/C line. The image and accompanying graph of linescan clearly shows that not all actin SF closely apposed to the nuclear surface form ALL lines. **A'.** Fluorescent intensity graph of linescan taken at the dashed yellow line using X position = 0 at the center of the ALL line. **B.** Actin and LaminA/C concentrate to form a linear structure. TPR labeled NPC flanking the actin/LaminA/C line can align with a railroad track orientation along the ALL line. **B'.** Fluorescent intensity graph of linescan taken at the dashed yellow line using X position = 0 at the center of the ALL line. **C.** Nucleoporin Pom121, also accumulates and is brighter in NPCs along ALL lines. **C'.** Fluorescent intensity graph of linescan taken at the dashed yellow line using X position = 0 at the center of the ALL line. **D.** LINC complex protein SUN2 and antibody FG414, which labels Nup153 and other FG-domain containing nucleoporins, also concentrates along ALL lines. **D'.** Fluorescent intensity graph of linescan taken at the dashed yellow line using X position = 0 at the center of the ALL line.

Next, we wanted to understand why the discrete Spots/NPCs are brighter. Is there a change in stoichiometry due to addition of specific nucleoporins, or are we seeing clustered grouping or clumping of multiple NPCs or addition of subunits. Therefore, we next asked whether we observed a heterogeneous change in fluorescent intensity for different nucleoporins in ALL proximal NPCs. To do this, we calculated the ratio of average fluorescent intensity for Near Spots/NPCs to average fluorescent intensity of Far Spots/NPCs. We found that all three labeling groups we tested were consistently 0.3X brighter in the region proximal to the ALL line (Figure 3C). Taken together, these results suggest no heterogeneity in the change in brightness based on the nucleoporin measured. While

this is clearly not an exhaustive survey, this result suggests that we are not likely observing significant alteration in the stoichiometry of individual nucleoporins. In addition, the incremental increase observed argues against this being a cluster of pores.

#### 2.4. NPCs dynamically accumulate and brighten on ALL lines

To understand the dynamics of NPC recruitment to ALL lines and why the ALL-proximal NPCs might be brighter, we performed live imaging of NPC recruitment to ALLs using fluorescent-tagged proteins and confocal microscopy. For these experiments, we followed spontaneously forming

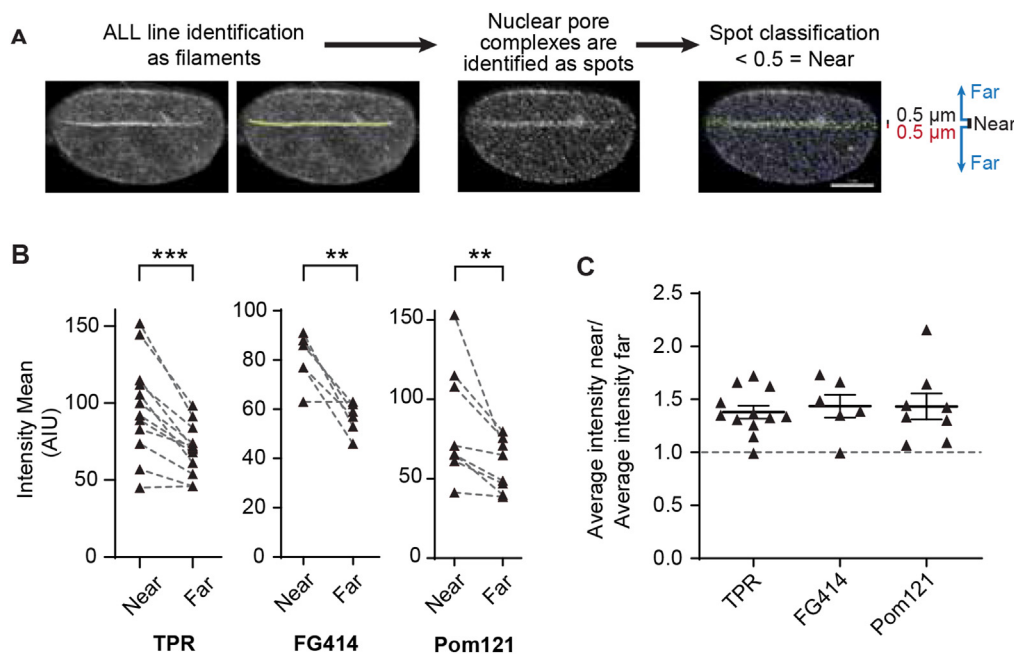


**Figure 3.** Nuclear pore complexes proximal to ALL nuclear lines are fluorescently brighter than NPCs that are distal. Cells for these studies were subjected to cyclic stretch, then fixed and antibody labeled. A. MATLAB ‘Filaments’ plugin for Imaris (Bitplane) was used to model three-dimensional linear structures overlaying ALL lines identified by concentrated linear LaminA/C and/or SUN2 and actin. MATLAB ‘Spots’ plugin in Imaris was used to reliably identify NPCs. NPCs were then sorted into Near ( $< 0.5\mu\text{m}$ ) and Far ( $> 0.5\mu\text{m}$ ) bins relative to the ALL line. Mean intensities of NPCs in each bin are compared in b. B. Pairwise quantitative comparison of the mean fluorescent intensity of NPCs proximal to the ALL line ( $< 0.5\mu\text{m}$ ) versus distal to the ALL line ( $> 0.5\mu\text{m}$ ) for nucleoporins TPR, FG414 and Pom121. C. Proportion of intensity near vs far is consistent between nucleoporins.

ALLs. We used Pom121-GFP to label the NPCs and the cell-permeable dye SiRActin to label the F-actin. We observed that the ALL line sweeps across the surface of the nucleus, accumulating NPCs as it progresses (Figure 4A and Movie S4). This is also evident with other approaches to labeling actin (Movie S5). The SF stays on the surface of the nucleus, and does not invaginate the surface of the nucleus as seen in this 300 nm thick Z-section. To visualize the results of this movement, we took orthogonal sections of the region of the ALL line. As the SF picks up NPCs, they appear to cluster or clump, as seen in the YZ slice (Figure 4B). When we measure the fluorescent intensity change over time using a linescan perpendicular to the ALL line, we see increasing brightness of the clustering NPCs (Figure 4C and 4D).

### 2.5. SUN1 is concentrated on ALL nuclear lines

These data suggest a model wherein mechanical force triggers SF formation and thickening, resulting in ALL line formation. As the actin is connected to the LINC proteins and intranuclear lamins, the lateral movement over the surface of the nucleus results in NPCs in the nuclear membrane being recruited to these structures. Consequently, this mechanical disturbance leads to the subsequent accumulation and altered composition of NPCs (Figure 4E).

The accumulation of NPCs on ALL lines raises the question of how the NPCs are tethered at the ALL lines. One candidate molecule that might be involved in connecting the NPCs to the ALL lines is SUN1 (Liu et al., 2007). SUN1 is a LINC complex protein that was previously shown to be essential for maintenance of the normal monodispersed distribution of NPCs on the surface of the nucleus (Liu et al., 2007). SUN1 was also reported to be required for interphase NPC assembly and to interact transiently with the nucleoporin Pom121 (Talamas and Hetzer, 2011), as well as with Nup153 (Li and Noegel, 2015).

If SUN1 were involved in recruitment or stabilization of NPC association with ALL lines, we would expect it to accumulate on ALL lines however; this had not been previously reported. To evaluate the sub-cellular distribution of SUN1 under conditions that promoted ALL line formation, we generated a fluorescent-tagged SUN1 (SUN1-mScarlet) and performed imaging to see if SUN1 concentrates at ALL lines. We found that SUN1 is present and concentrated at ALL lines and displays a distribution that appears to be coincident with NPCs that are accumulated at ALL lines (Figure 4F), thereby presenting SUN1 as a candidate for linking NPCs to ALL lines.

### 2.6. Generating SUN1 CRISPR knockdown and knockout cell lines to characterize the role of SUN1 in recruiting NPCs to ALL lines

To test the hypothesis that SUN1 might be required for the ability of NPCs to concentrate along ALL lines, we generated a CRISPR knockout of the *SUN1* gene (Figure 5A) in mouse embryo fibroblasts (MEFs). One challenge in deploying CRISPR technology for gene disruption is stably mutating both copies of the gene. To address this concern, we utilized a dual-antibiotic strategy that employed homology directed repair (HDR) to target insertion of two different antibiotic resistance mutagenic cassettes, one for Blasticidin and one for Neomycin (Supharattanasitthi et al., 2019) and a stop codon to the sequence of *SUN1* (Figure 5B). This allowed selection of cells that had received both inserts by treating cells sequentially with the two antibiotics. In addition to the dual antibiotic HDR targeting approach, we also sought to increase the specificity and efficiency of our mutagenesis by using single stranded DNA for targeting (Li et al., 2017). This approach enabled us to identify cells with cassettes inserted in both copies of the gene. Following expression of the mutagenic transgene, we cultured cells that survived treatment with both antibiotics, and then used serial dilution to generate clonal cell lines founded on a single cell (SUN1KD-G7). To test for the presence of SUN1, we performed Western blots and immunofluorescent labeling for SUN1 (Figures 5D and 5E and Figure S1). These showed decreased but not completely absent SUN1 labeling, indicating we had succeeded in generating a knockdown “SUN1KD-G7”, but had not succeeded in generating a protein null cell line (Figure 5D and 5E). In studying the sequence of *SUN1*, we established that we had disrupted one start codon, but that there was another start sequence downstream 37 amino acids of our initial target in Exon 3 (Figure 5A). We hypothesized that this remaining start codon was responsible for the persistent SUN1 protein production. To generate a complete knockout, therefore, we designed another HDR targeting sequence using double strand linear DNA to insert antibiotic resistance cassettes for Zeocin and HygromycinB (Figure 5C). We applied this secondary knockout strategy to our SUN1 knockdown cells. This proved to be a highly effective approach. Of 26 recovered dual antibiotic resistant clonal cell lines, all showed a complete lack of SUN1 protein in the western blot (Figure 5D). We confirmed this immunoblot finding using indirect immunofluorescent labeling of SUN1 (Figure 5E). The nuclear rim is detectable in WT and even a little in the knockdown, KD-G7, but is not detectable in the knockout SUN1KO-C11 cells.

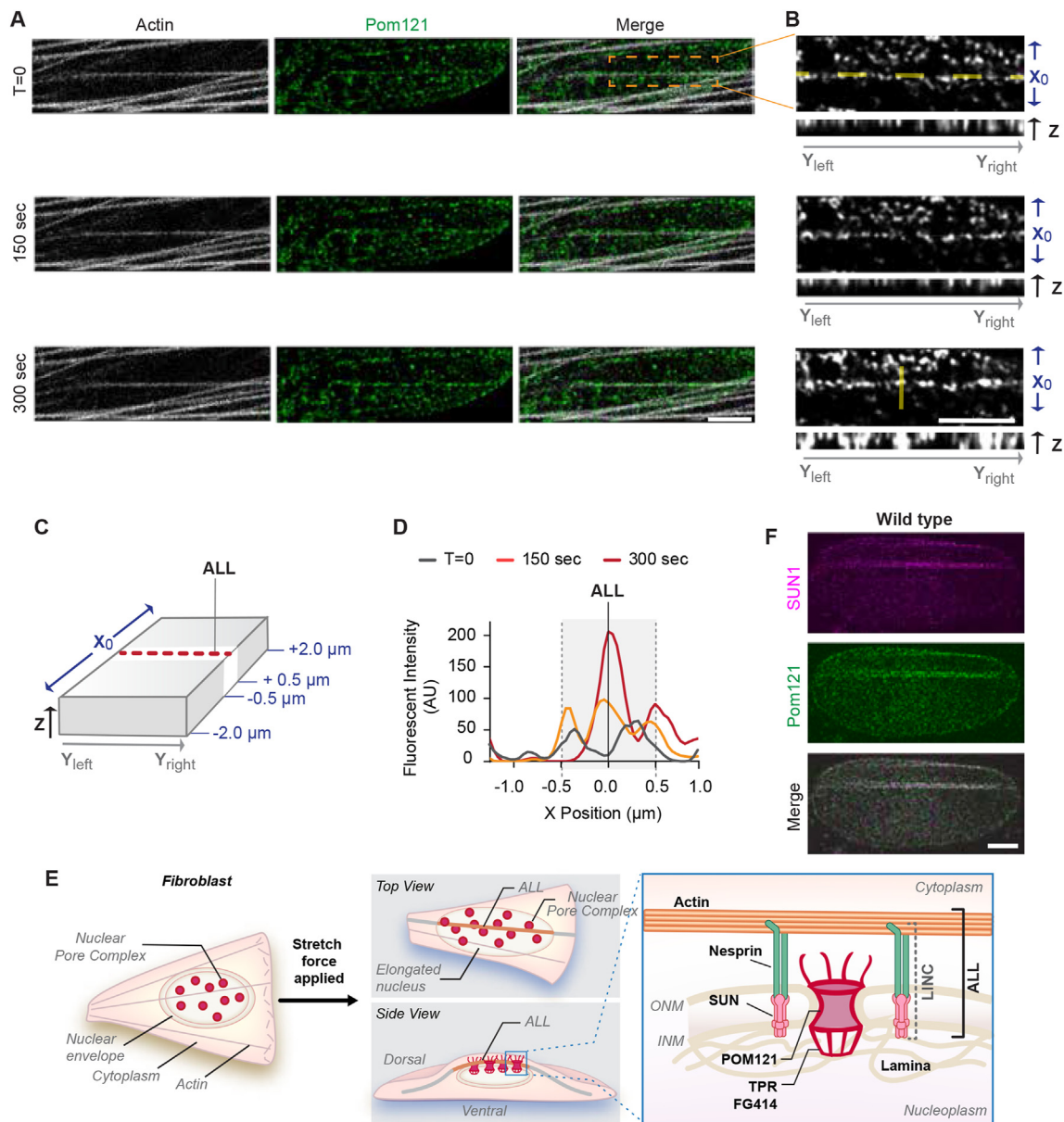


**Figure 4.** Nucleoporin fluorescent signal increases upon joining nuclear lines. (Live cell) Visualizing fluorescent intensity changes in NPC when accumulating on ALL lines using live imaging. NPCs become larger and fluorescently brighter as they accumulate on the ALL line. A. As the actin SF sweeps across the surface of the nucleus, NPCs, labeled with Pom121-GFP accumulate on the structure and show increased fluorescent intensity as NPC accumulate. B. Enlarged single 300nm thick Z plane of the boxed area in a) with accompanying ZY plane (below) taken at the yellow dotted line overlaying the ALL line. C. Schematic showing orientation of the imaging planes and region of fluorescent intensity measurement. D. Linescan at three timepoints of fluorescent intensity through NPC accumulation. E. Formation of ALL lines results in the clustering of NPCs on ALL lines. F. SUN1 concentrates at ALL lines with Pom121.

With the *SUN1* knockdown and *SUN1* knockout clonal cell lines in hand, the next step was to evaluate whether interference with *SUN1* levels had an impact on the formation of ALL lines. To test this, we imaged labeled actin and laminaA/C in *SUN1*KO-C11 knockout cell line. We found that ALL line formation was preserved in the absence of *SUN1* as by actin and laminaA/C distribution (Figure 5F).

### 2.7. Disruption of *SUN1* reduces NPC localization to ALLs visualized by live cell imaging

We next explored whether cells with compromised *SUN1* expression showed any deficit in NPC accumulation on ALL lines. We performed live cell imaging to compare NPC dynamics between Wild Type parental cells, *SUN1* knockdown cells (*SUN1*KD-G7), and *SUN1* knockout cells

(*SUN1*KO-C11). We used Hoechst dye to identify nuclei, mN2G-GFP to identify ALL lines, Pom121-mScarlet to label NPCs and the dye-based actin label SiRActin to identify actin SFs. We imaged every minute for a 1-h period, and then reviewed for ALL line occurrences. Consistent with the above findings in which we monitored actin and laminaA/C markers of ALL lines (Figure 5F), we observed formation of ALL lines as evidenced by linear mN2g-GFP signal coordinated with actin SFs (Figure 6A), thus demonstrating that the actin, LINC complex, and laminaA/C constituents of ALL lines appeared unperturbed in cells with *SUN1* deficits. However, we observed a significant diminution of the NPC signal on ALL lines in both the knockdown G7 and knockout C11 cells (Figure 6A). To quantify this change we established the track of the ALL lines using the MATLAB Filaments function in Imaris. These linear elements were then broken into 250  $\mu$ m Spots using the Spots function in Imaris. Fluorescent

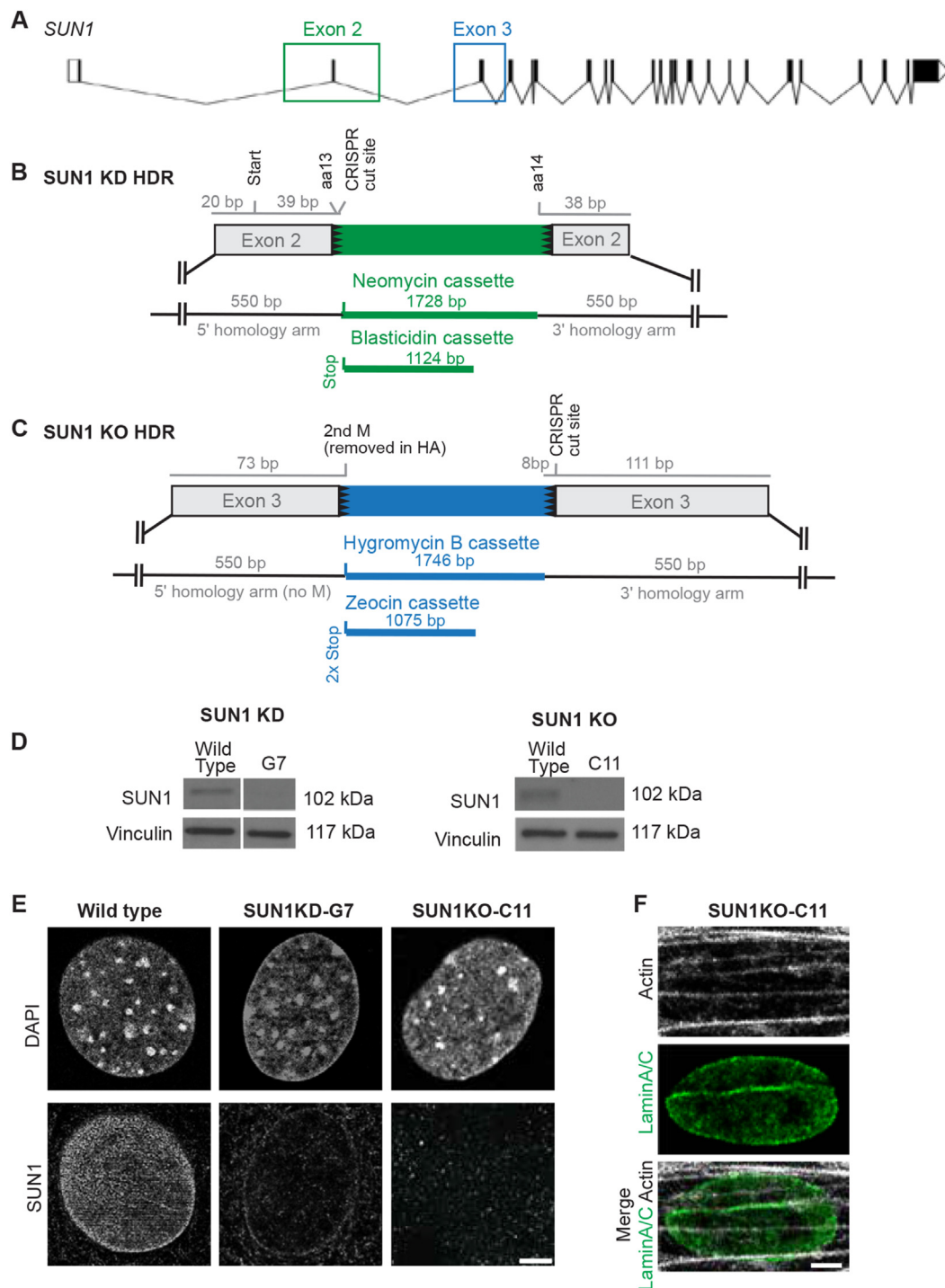


**Figure 5.** Generating SUN1 CRISPR knockdown and knockout cell lines for studying the role of SUN1 in localization of NPCs to ALL lines. **A.** Intron/exon diagram of SUN1 gene showing location of the CRISPR HDR insertion sites. **B.** Map of CRISPR HDR insertion into SUN1 exon 2 that led to knockdown of SUN1. Insertion cassettes, each with one of two different antibiotic resistance elements, Neomycin or Blasticidin, allowed for identification of cells where both DNA strands were successfully targeted. **C.** Map of CRISPR HDR insertion into SUN1 exon 3 that led to a protein null knockout of SUN1. Insertion cassettes with different antibiotic resistance elements, HygromycinB or Zeocin, allowed for identification of cells where both DNA strands were successfully targeted. The cells used for the exon 3 targeting were cells previously mutagenized at exon2. **D.** Following establishment of stable monoclonal cell lines, western blots showing successful SUN1 knockdown G7 and knockout C11. Vinculin was used as the loading control. **E.** Images of cell nuclei showing the significant knockdown, and complete knockout of SUN1 correspondingly in the knockdown and knockout cell lines. **F.** LaminA/C and actin form ALL lines in SUN1 knockout cells, showing disruption of SUN1 does not interfere with the formation of ALL lines.

intensities within the Spots are used to calculate means for each Spot, thereby generating incremental intensity means along the length of the Filaments. We then averaged five time points along the region of peak ALL line labeling.

To further rule out the possibility that the reduction in NPC association with ALL lines in the SUN1 mutants was due to a deficit in the integrity of the ALL lines, we conducted a quantitative analysis of the fluorescence intensity of mN2G-GFP on ALL lines in wild-type or SUN1-

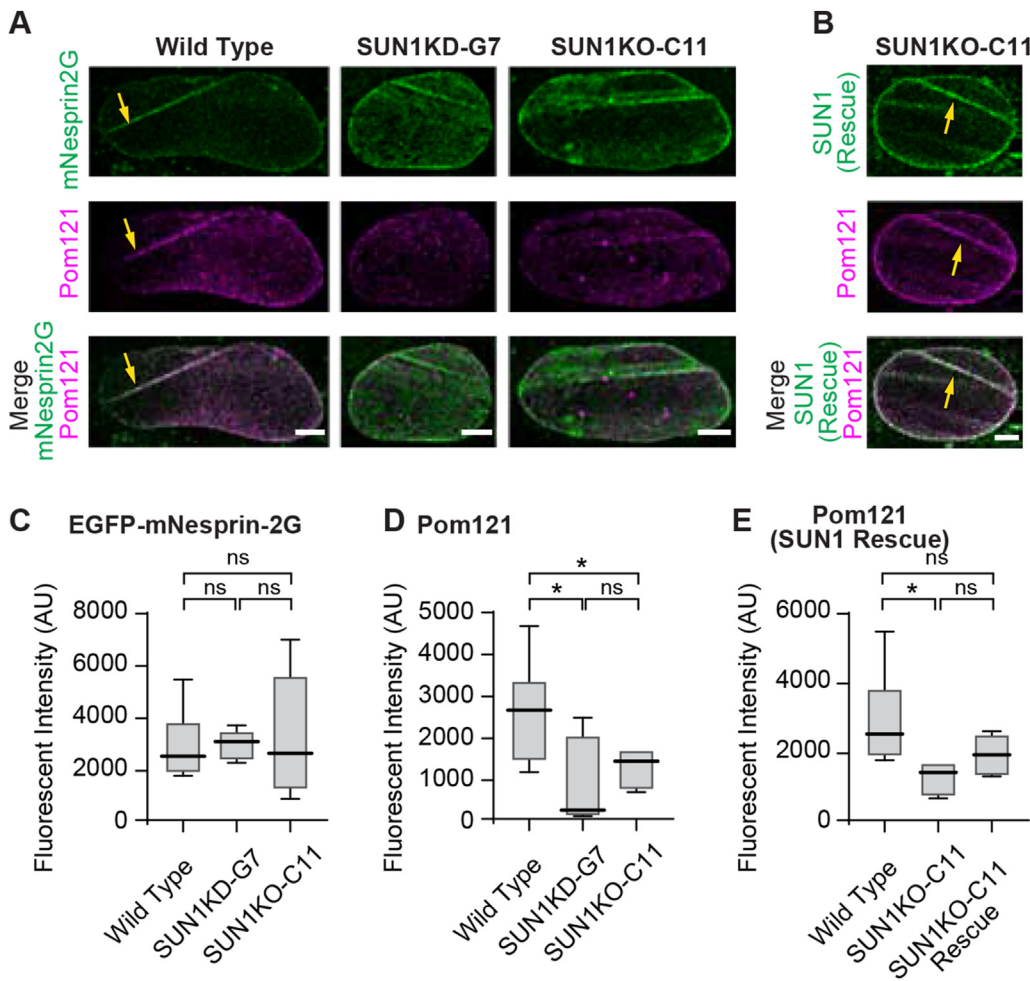


**Figure 6.** *SUN1* gene disruption leads to abrogated NPC accumulation at ALL lines in live cell imaging studies. ALL lines are maintained in *SUN1* knock-down or knockout cells. Pom121 signal is restored with Sun1 rescue. **A.** Confocal images of live cells with transiently expressed EGFP-mN-2G and Pom121-mScarlet. Yellow arrows show locations of ALL lines. EGFP-mN-2G identifies the location of the ALL lines. Pom121 signal shows the NPC localization to the ALL line, which is abrogated in the *SUN1* knockdown and knockout cells. **B.** Transient expression of *SUN1* shows phenotypic rescue via restoration of Pom121 signal at the ALL line. **C.** EGFP-mN-2G levels are maintained on nuclear lines in wild type ( $n = 6$ ), *SUN1* knockdown ( $n = 5$ ) and *SUN1* knockout ( $n = 6$ ) cells, indicating no decrease in the robustness of ALL lines with decrease or loss of *SUN1* function. **D.** Pom121-mScarlet levels on ALL lines in wild type ( $n = 6$ ), *SUN1KD-G7* ( $n = 5$ ), *SUN1KO-C11* ( $n = 6$ ) show a significant decrease in signal in the *SUN1* mutants, indicating abrogation of NPC accumulation. **E.** Pom121-mScarlet levels on ALL lines shows complete rescue of signal with transient expression of *SUN1*.

deficient cells (Figure 6B and 6C). We found that in both the *SUN1KD-G7* knockdown and *SUN1KO-C11* knockout, the mN2G-GFP fluorescence levels on ALL lines appeared comparable to Wild Type cells (Figure 6C), suggesting there had been no attenuation of ALL line formation in the mutants. However, when we compared the mean intensities of Pom121-mScarlet between the Wild Type and *SUN1* mutant cells, we saw a significant drop in fluorescent intensity in both the *SUN1KD-G7* knockdown cells and *SUN1KO-C11* knockout cells (Figure 6D), which was restored with transient expression of *SUN1* (Figure 6E), confirming that a *SUN1* deficiency compromises the accumulation of the NPC component, Pom121, on ALL lines.

### 2.8. Disruption of *SUN1* reduces NPC localization at ALL lines in stretch stimulated fixed cells

To further characterize the requirement of *SUN1* for NPC recruitment to ALL lines, and to rule out any artifacts that might result from the transient expression of fluorescent NPC and ALL line constituents, we analyzed populations of cells exposed to uniaxial cyclic stretch prior to fixation and antibody labeling. This allowed us to characterize the behavior of large numbers of cells and to monitor endogenous proteins for their association with ALL lines downstream of stretch. We plated Wild Type, *SUN1KD-G7* or *SUN1KO-C11* and *SUN1KO-C11* cells rescued with transiently expressed *SUN1*-GFP on silicone membranes. We subjected each population of cells to 1 h of 15% uniaxial cyclic stretch at 0.5 Hz. We then fixed the cells and used indirect immunofluorescence to visualize cell structures. DAPI and Phalloidin were used to identify nuclei and actin SFs. The ALL lines were labeled with an

antibody to the LINC complex protein *SUN2*. NPCs were labeled with the FG414 antibody for FG-containing nucleoporins. As with the live imaging experiments, we observed that ALL line formation was preserved in *SUN1* mutant cells, as evidenced by the maintenance of *SUN2* signal coordinated with actin SFs (Figure 7A). However, we saw a clear loss of NPC recruitment to the ALL lines (Figure 7A). The loss of NPC colocalization in *SUN1* knockout cells was apparently rescued by re-expression of the *SUN1*-GFP transgene (Figure 7B). As with the live imaging analysis, we used the Imaris Filaments function to identify and isolate the tracts of the ALL lines. We then recorded incremental intensity data for the *SUN2* and the FG414 signals. We first determined whether ALL line formation had been diminished in the *SUN1* knockdown or knockout cells when compared to Wild-Type cells by comparing *SUN2* levels on ALL lines in all three genotypes and found no loss of *SUN2* signal on the ALL lines (Figure 7C). We then compared FG414 signals along these same tracts and found a significant decrease in FG414 signal in the *SUN1* knockdown cells, and an even greater decrease in the *SUN1* knockout cells (Figure 7D). To attempt to rescue the *SUN1* loss of function phenotype in the *SUN1* knockout cells, we expressed *SUN1*-GFP using transient transfection. We found that accumulation of NPCs along ALL lines was completely restored in *SUN1* knockout cells expressing the *SUN1*-GFP transgene (Figure 7B and D).

Together these data show that partial loss of *SUN1* results in a reduction of NPC recruitment to ALL lines and complete loss of *SUN1* results in a significantly greater loss of NPC recruitment at ALL lines. The complete rescue of this phenotype with re-expression of *SUN1* indicates the loss of NPC clustering at ALL lines in these *SUN1* mutant cell lines is specific to the loss of *SUN1*.

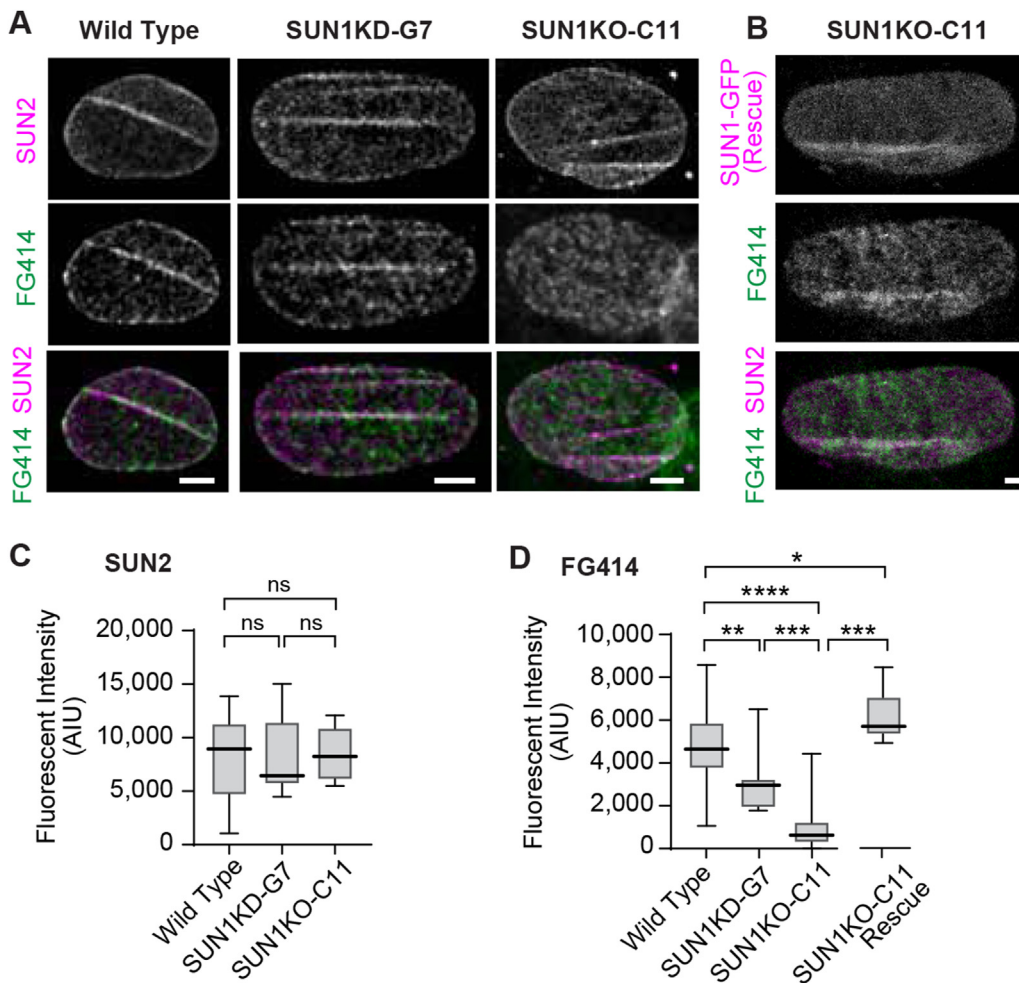


**Figure 7.** *SUN1* gene disruption leads to significantly abrogated NPC accumulation at ALL lines. In cells subjected to cyclic stretch, mutation of *SUN1* results in no loss of ALL lines, as shown by *SUN2* levels, but does result in loss of NPC accumulation on ALL lines. Transient expression of *SUN1*-GFP fully rescues *FG414* fluorescent intensity levels on ALL lines in *SUN1* knockout cells. **A.** Cells subjected to cyclic stretch, fixed and antibody labeled for *SUN2* to identify ALL lines, and *FG414* to identify NPCs. **B.** Rescue of *SUN1* knockout (C11) with transiently expressed *SUN1*-GFP restores accumulation of NPC accumulation near ALL lines. **C.** Mean *SUN2* levels on ALL lines to compare ALL line formation in wild type (N = 16) to *SUN1*KD-G7 (N = 15) and *SUN1*KD-C11 (N = 10) cell lines. **D.** *FG414* labeling levels in wild type (N = 14), *SUN1*KD-G7 (N = 17) and *SUN1*KO-C11 (N = 17) shows loss of normal NPC accumulation at ALL lines. Transient re-expression of *SUN1*-GFP in *SUN1*KO-C11 (N = 10) cells shows rescue of knockout phenotype.

### 3. Discussion

In this work, we provide new insights regarding the response of cells to mechanical stress, with a focus on the impact of mechanical cues on the architecture of the nuclear envelope. We present live cell dynamic analysis of the formation of ALL lines in response to mechanical stretch. We show that the LINC complex protein components of these structures are guided in their linear formation by SFs that have already formed and are in contact with the surface of the nucleus. Additionally, nuclear envelope proteins N-2G and *SUN2* arrive simultaneously with NPCs. NPCs cluster near ALL lines in response to stretch as well as in response to normal force changes within the cell. When NPCs are concentrated in a 1  $\mu\text{m}$  region flanking the ALL line, fluorescent-labeled nucleoporins appear brighter than in NPCs dispersed on the surface of the nucleus. This does not appear to be due to changes in the stoichiometry of specific nucleoporins, as we do not see differences in fluorescent intensity increases among the multiple nucleoporins evaluated. Several possible explanations for the increased fluorescence intensity are plausible, including aggregation of NPCs or conformational changes in ALL line-associated NPCs. High resolution approaches such as superresolution will be required to fully elucidate the conformational or compositional changes this work suggests (Sabinina et al., 2021; Schuller et al., 2021; Zimmerli et al., 2021).

Based on the striking accumulation of NPCs proximal to ALL lines in response to mechanical cues, we sought to identify the molecular mechanism that accounted for the altered distribution of the NPCs. We proposed and tested the hypothesis that *SUN1* is responsible for normal recruitment of NPCs to ALL lines. Using CRISPR gene targeting strategies to knock down and knock out *SUN1* in cells, we demonstrated that *SUN1* is required for the stretch-induced accumulation of NPCs at ALL lines.

The failure of NPCs to concentrate at ALL lines downstream of cyclic stretch in *SUN1*-null cells is not explained by a failure to establish robust ALL lines since actin, mN2G, *SUN2* and laminaA/C accumulation at ALL lines persists at wild type levels in the *SUN1* KO cells. We confirmed the specificity of these CRISPR *SUN1* disruptions for the decreased NPC accumulation phenotype by rescuing NPC accumulation at ALL lines with exogenous re-expression of *SUN1*. Taken together, these data suggest a model in which ALL nuclear lines form in response to mechanical force, and NPCs cluster near these ALL lines in a *SUN1* dependent manner (Figure 8). In addition to this, the ability to disrupt recruitment to ALL line via reduction or elimination of *SUN1* function provides clear indication that our observation of NPC concentration at ALLs is not due to an imaging artifact from formation of an indentation in the surface of the nucleus. This is further reinforced by our ability to rescue recruitment through transient reexpression of *SUN1*.

The nucleus responds to mechanical force (Maniotis et al., 1997b) and can be viewed as a cellular mechanosensor (Kirby and Lammerding, 2018). NPCs perforate the nuclear membrane providing an exquisitely regulated portal for the bidirectional transit of macromolecules between the cytoplasm and the nucleoplasm. Previous work in our lab and other labs detailed the role of stretch regulation of growth factor signaling including transcription factors YAP/TAZ and MRTF (Aragona et al., 2013; Driscoll et al., 2015; Elosegui-Artola et al., 2017; Hoffman et al., 2020). These changes in transport across the nuclear membrane are postulated to occur, in part, as a direct result of forces exerted on NPCs (Elosegui-Artola et al., 2017).

ALL lines are essential links in the chain of mechanical connection between the cell's environment and the genetic material: extracellular matrix to focal adhesions to SFs to LINC complex proteins to lamins and

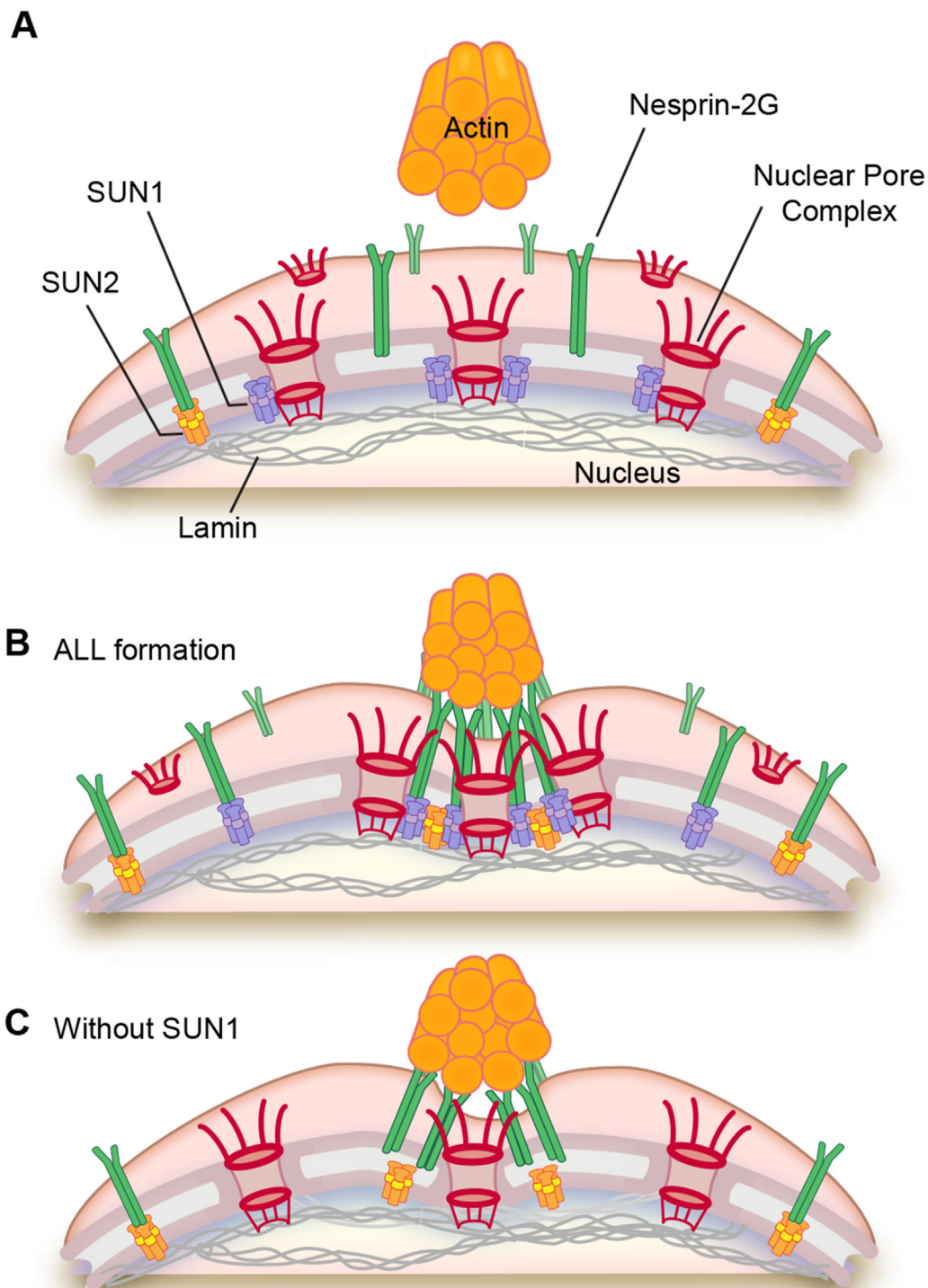


**Figure 8.** Model shows the role of SUN1 in accumulation of NPCs at ALL lines. A. Shows wild type state prior to stretch. B. Shows wild type following stretch. Actin SF is interacting with N-2G. SUN1 is interacting with the NPCs. C. Stretched but without SUN1. The actin SF are still connected to the N-2G, but the NPCs are dispersed.

associated proteins to chromatin (Maniotis et al., 1997b; Stewart-Hutchinson et al., 2008). Consequently, the force-regulated recruitment of NPCs to these sites suggests this function has a role in the integration of molecular response to mechanical input. Our observation that ALL line-associated NPCs are altered in a manner that results in an increased fluorescent signal from labeled nucleoporins constituents may provide clues to how transmission through NPCs may be altered in a force dependent manner. We have observed the possible accumulation of NPCs as external forces and SF contraction move the ALL line over the nuclear

surface, there are likely additional changes occurring such as the addition of subunits. It is possible that multiple NPCs are clustering, leading to locally increased force transmission across the membrane. It is unclear how the clustered NPCs we observe are arranged, but they may be multimerizing or undergoing significant composition changes. As precedent for this, other groups have shown both the stoichiometry and subunit composition of NPCs may change (Rabut et al., 2004; Rajoo et al., 2018), indicating the possibility of a high level of stoichiometric and structural flexibility in NPCs.

The novel finding that SUN1 is concentrated along ALL lines and serves to immobilize NPCs may be particularly important in terms of understanding the role of cytoskeletal force in regulating NPC size as well as pore constriction and dilation. SUN1 and SUN2 may have some functional redundancy, but they also have key structural and functional differences (Hennen et al., 2018; Jahed et al., 2018a, 2018b; Jahed and Mofrad, 2019; Ostlund et al., 2009). SUN2 is a central component of TAN lines (Luxton et al., 2010, 2011), while SUN1 has not previously been observed on nuclear lines. Within the nucleus, SUN2 binds to nuclear A-type lamins (Ostlund et al., 2009). This interaction serves to limit SUN2's mobility within the nuclear membrane (Liang et al., 2011). The homologue SUN1 is also embedded in the nuclear membrane and has a strong interaction with A-type lamins, which limits its mobility in the nuclear membrane (Liu et al., 2007; Ostlund et al., 2009). However, unlike SUN2, SUN1 does not appear to have a role in limiting the mobility of N2G (Liu et al., 2007; Ostlund et al., 2009).

While both SUN1 and SUN2 anchor to both chromatin and nucleoplasmic lamins, SUN1, but not SUN2, serves to prevent NPC clumping. This is evidenced by NPC clustering, as opposed to a normal mono-dispersed distribution, that occurs when either SUN1 is depleted via RNA interference, or when a dominant-negative SUN1 is expressed (Liu et al., 2007). Additionally, dispersed NPCs colocalize with SUN1 but not SUN2 (Lu et al., 2008). Importantly, we demonstrate a new role for SUN1 in the recruitment of NPCs in response to mechanical cues.

This work suggests force induced recruitment of NPCs to ALLs may play a significant role in mediating the cellular response to mechanical force. While the means of linkage between SUN1 and NPCs has yet to be determined, the interaction between SUN1 and NPCs at ALL lines may provide a new opportunity for examining the complex relationship between LINC complexes and NPCs (Jahed et al., 2016). One possible model might be that clustering of NPCs brings them into proximity with transcriptional targets relevant to mechanotransduction. Additionally, the transfer of force from SFs to NPC may alter the patency of the nuclear pore, thereby altering the flow of growth factor signaling molecules into the nucleus. While recent work has reinforced the theory that force alters NPC function (Elosegui-Artola et al., 2017; Hoffman et al., 2020) the mechanism for altering the contraction and dilation of the nuclear pore is unclear. Consequently, this work provides a foundation and reagents for progressing our understanding of how mechanical signals are converted into chemical signals. Future investigation into the function of NPCs linked to ALL lines may provide insight into the regulation of NPCs based on the input of cytoskeletal force. In summary, this work suggests new opportunities for studying the dynamic changes in the localization, distribution, composition and function of NPCs in response to mechanical stress.

## 4. STAR methods

### 4.1. Resource availability

#### 4.1.1. Lead contact

Further information and requests for resources and reagents should be directed to and will be fulfilled by the lead contact, Mark Smith ([mark.smith@hci.utah.edu](mailto:mark.smith@hci.utah.edu)).

#### 4.1.2. Materials availability

Plasmids generated in this study have been deposited to Addgene (pcDNA-Pom121 mApple (#187674), pcDNA-SUN1 EGFP (#187675), pcDNA-SUN1 mApple (#187676), pcDNA-SUN1 mScarlet (#187677), pcDNA-SUN2 EGFP (#187678), pcDNA-SUN2 mApple (#187679), pCMV-Pom121 GFP (#187680), pCMV-Pom121 mScarlet (#187681), pCMV-SUN1 GFP (#187682), pCMV-SUN1 mScarlet (#187683), pCMV-SUN2 GFP (#187684), pCMV-SUN2 mScarlet (#187685), pLenti-Lifeact EGFP (#187686), pLenti-Lifeact mApple (#187687)).

CRISPR knockout and tagged mouse cell lines generated in this study are available upon request.

**4.1.2.1. Data and code availability.** The authors are willing to share all of the data. No original code was generated for this paper.

All fixed cell and live imaging image data reported in this paper will be shared by the lead contact upon request.

### 4.2. Code

This paper does not report original code.

Any additional information required to reanalyze the data reported in this paper is available from the lead contact upon request.

### 4.3. Experimental model details

#### 4.3.1. Cell culture

WT mouse fibroblast cells were isolated and cultured as previously described (Hoffman et al., 2006). Cells were cultured in high-glucose DMEM (#11965) supplemented with sodium pyruvate (#11360070), L-glutamine (#25030081), penicillin/streptomycin (#15140122) from Invitrogen, and 10% fetal bovine serum (FBS; Hyclone Labs, Logan, UT). Transient transfections for SUN1 KO and fluorescently labeled proteins were performed using Lipofectamine 2000 transfection reagent (Invitrogen #11668). Briefly, 4 µg of DNA was diluted in 250 µl of Opti-MEM I Reduced Serum Medium (Invitrogen #31985). 10 µl of Lipofectamine 2000 was diluted in 250 µl of Opti-MEM I Reduced Serum Medium and incubated 5 min at room temperature. The diluted plasmids and diluted Lipofectamine 2000 were mixed gently, incubated 30 min at room temperature and then added to the cells plated at 80% confluency in DMEM without antibiotics in one well of a 6 well plate. Time lapse imaging of live cells transfected with fluorescent proteins was performed 2–5 days post transfection. Live un-stretched cells were incubated in SiR-Actin (250 nM) for 1 h prior to imaging to visualize F-actin. Transient transfections for SUN2 EGFP/mApple CRISPR experiments were performed using FuGENE HD transfection reagent (Promega E2311). Briefly, 2 µg CRISPR-Cas9 DNA and 2 µg SUN2 EGFP/mApple HDR DNA were added to 1200 µl DMEM without supplements or antibiotics. 60 µl of FuGENE HD was added to DNA/DMEM mix and incubated at room temperature for 30 min before adding dropwise to 130 k cells plated in 10 cm dish in supplemented DMEM.

#### 4.3.2. Immunofluorescence reagents

The following antibodies and staining reagents were used including dilutions/concentrations: Primary antibodies: lamin A/C (#4777; 1:150) from Cell Signaling Technology; nucleoporins FG414 (#50008; 1:250), SUN2 (#124916; 1:150) from Abcam, POM121 (GTX-102128; 1:100) from GeneTex; TPR (IHC-00099; 1:250) from Bethyl Labs; SUN1 (MABT892; 1:50 IF; 1:100 WB), vinculin (V-9131; 1:20,000) from Sigma. Secondary antibodies: Alexa Fluor goat anti-mouse 568 (A-11031; 1:200), Alexa Fluor goat anti-rabbit 488 (A-11008; 1:200), Alexa Fluor goat anti-rabbit 568 (A-11036; 1:100), Alexa Fluor goat anti-mouse 647 (A-21236; 1:500), Alexa Fluor goat anti-rabbit 647 (A-21245; 1:500) from Thermo Fisher Scientific; goat anti-rabbit CF568 (20102-1; 1:200), goat anti-mouse CF568 (20100-1; 1:200) from Biotium; Cy3B (PA63101; 1:50) from GE Healthcare conjugated according to manufacturer protocol to donkey anti-mouse IgG (#715-005-150) from Jackson ImmunoResearch. Staining reagents: Alexa Fluor phalloidin 488 (A-12379; 1:200), Alexa Fluor phalloidin 568 (A-12380; 1:200), Alexa Fluor phalloidin 647 (A-22287; 1:100), DAPI (D1306; 0.1 µg/ml), Hoechst 33342 (H1399; 5 µg/ml) from Thermo Fisher Scientific; SiR-Actin (CY-SC001; 1 µM) from Cytoskeleton Inc.

#### 4.3.3. Cell fixation and staining for immunofluorescence imaging

Cells were fixed using 4% paraformaldehyde (Ted Pella, Inc #18505) in PBS for 15 min, permeabilized and blocked in 3% BSA, 0.3% Triton X-100 in PBS for 30 min at room temperature, probed 1 h at room temperature with primary antibody diluted in 1%BSA, 0.2% Triton X-100 in PBS, washed 3 × 3 min at room temperature in 0.05% Triton X-100 in

PBS, probed 1 h at room temperature with secondary antibody, DAPI, and SiR-Actin or phalloidin diluted in 1%BSA, 0.2% Triton X-100 in PBS, washed 3 × 3 min in 0.05% Triton X-100 in PBS, washed 3 × 3 min in PBS.

#### 4.3.4. PCR

Genomic DNA extractions from confluent 10 cm dishes of MEFs were performed using PureLink Genomic DNA Kit (Thermo Fisher K182001) according to manufacturer protocols. All PCR reactions except SUN2 EGFP/mApple CRISPR experiments were performed using Platinum SuperFi DNA Polymerase (Thermo Fisher 12351010) according to manufacturer protocols. SUN2 EGFP/mApple CRISPR PCR reactions were performed using Phusion High-Fidelity DNA polymerase (Thermo Fisher F530S) according to manufacturer protocols. SOE PCR was performed using a 1:1:1 M ratio of each PCR product to be spliced. An initial round of 20 cycles was performed minus the 5' and 3' primers containing the attB sites. Primers were then added followed by an additional 30 cycles. Final PCR product was run on a 1% agarose gel and the correct size band was gel purified and used in a Gateway BP reaction with pDONR221 to create an entry plasmid.

#### 4.3.5. Plasmids and cloning

**EGFP-mini-nesprin-2G DNA** was a gift from Gregg Gundersen.

**4.3.5.1. pcDNA-Pom121-mApple/EGFP, pcDNA-SUN1-mApple/EGFP, and pcDNA-SUN2-mApple/EGFP.** Cloned using Invitrogen's Multisite Gateway Cloning. L1R5 entry clones were created by PCR amplification of cDNAs for Pom121 (Transomic Technologies BC053101), SUN2 (Transomic Technologies BC098208), or SUN1 (OriGene MR211159) with 5' attB1 and 3' attB5r recombination sites. PCR products were gel purified and recombined with pDONR221 P1P5r plasmid (Invitrogen) to create L1R5 entry clones. An L5L2 Gateway entry clone was made for both mApple and EGFP by PCR amplification with 5' attB5 and 3' attB2 recombination sites. PCR product was gel purified and recombined with pDONR 221 P5P2 plasmid (Invitrogen) to create the entry clone. Pom121, SUN1, and SUN2 entry clones were recombined with either the mApple or EGFP entry clone and pcDNA6.2-DEST plasmid (Invitrogen) to create expression plasmids. BP reactions to create entry clones were performed using Gateway BP clonase II enzyme mix (Invitrogen #11789020). LR reactions to create expression clones were performed using Gateway LR clonase II enzyme mix (Invitrogen #11791020).

**4.3.5.2. pCMV-Pom121-GFP, pCMV-SUN1-GFP, and pCMV-SUN2-GFP.** Cloned into pCMV-GFP a gift from Connie Cepko (Addgene plasmid #11153) (Matsuda and Cepko, 2004). Pom121 and SUN2 cDNA's were PCR amplified with primers to add 5' XhoI and 3' AgeI restriction enzyme sites. PCR products and pCMV-GFP were digested with XhoI and AgeI, gel purified, and ligated to create expression plasmids. SUN1 cDNA was PCR amplified with primers to add 5' NheI and 3' SacII restriction enzyme sites. PCR product and pCMV-GFP were digested with NheI and SacII, gel purified, and ligated to create expression plasmid.

**4.3.5.3. pCMV-Pom121-mScarlet, pCMV-SUN1-mScarlet, and pCMV-SUN2-mScarlet.** Cloned into pLifeAct\_mScarlet\_N1 a gift from Dorus Gadella (Addgene plasmid #85054) (Bindels et al., 2017). Pom121 and SUN2 cDNA's were PCR amplified with primers to add 5' XhoI and 3' AgeI restriction enzyme sites. PCR products and pLifeAct\_mScarlet\_N1 were digested with XhoI and AgeI (removing the LifeAct sequence from the plasmid), gel purified, and ligated to create expression plasmids. SUN1 cDNA was PCR amplified with primers to add 5' NheI and 3' BamHI restriction enzyme sites. PCR product and pLifeAct\_mScarlet\_N1 were digested with NheI and BamHI (removing the LifeAct sequence from the plasmid), gel purified, and ligated to create expression plasmid.

**4.3.5.4. pLenti-Lifeact-mApple and pLenti-Lifeact-EGFP.** Cloned using Invitrogen's Multisite Gateway cloning. EGFP/mApple were amplified by PCR with a 5' attB1 and 3' attB2 recombination site. To the 5' attB1 primer the 51 bp Lifeact sequence (atgggtgtcgcagattgatcaagaaattcgaaagcatctcaaaggaagaa) was added to incorporate Lifeact directly upstream of either the mApple or EGFP sequence. PCR product was gel purified and recombined with a pDONR221 plasmid (Invitrogen) to create the L1L2 entry vector. This was then recombined with pLenti6.3-DEST (Invitrogen) to create the expression plasmid.

#### 4.3.5.5. SUN1 CRISPR antibiotic resistance homology directed repair (HDR).

Antibiotic resistance gene templates for the creation of HDR constructs were obtained from the following plasmids that were a gift from Peter Jon Nelson (Jäckel et al., 2016) pSBDEST.B (Addgene #79460); pSBDEST.N (Addgene #79468); pSBDEST.H (Addgene #79464); pSBDEST.Z (Addgene #79470). To create an antibiotic resistance gene "cassette" the antibiotic resistance genes plus the SV40 promoter and SV40 Poly(A) signal were PCR amplified from the plasmid. The 5' primer included 30 bp homology to the 5' homology arm (HA) for SUN1 including added stop codon(s) and the 3' primer included 30 bp homology to the 3' HA for SUN1. 550 bp of 5' HA SUN1 genomic DNA was PCR amplified with the addition of a 5' attB1 site and 3' stop codon(s) plus 30 bp homology to the antibiotic resistance gene cassette promoter. 550 bp of 3' HA SUN1 genomic DNA was PCR amplified with a 5' addition of 30 bp homology to the 3' sequence of the antibiotic resistance gene cassette Poly(A) signal and a 3' addition of an attB2 site. The three separate PCR products were then gel purified and an SOE PCR reaction was performed to create an attB1-SUN1 5' HA-stop(s)-antibiotic resistance gene cassette-SUN1 3' HA-attB2 product. Product was gel purified and subsequently used in a BP reaction with pDONR 221 (Invitrogen) to create a Gateway entry plasmid. To avoid the insertion of unwanted plasmid backbone DNA into the genome the plasmid was then used as a PCR template to create single stranded DNA through Lambda exonuclease (Thermo Scientific EN0561) digest of PCR product (per manufacturer's protocol) or undigested double stranded DNA of only the 5' HA SUN1-antibiotic resistance gene-3' HA SUN1 portion of the plasmid. PCR primers were located at the 5' end of the 5' HA and the 3' end of the 3' HA of SUN1. For the Lambda exonuclease digest the 3' antisense PCR primer was 5' phosphorylated. Single or double stranded HDR DNA and the CRISPR-Cas9 plasmid were then transiently transfected into cells to perform the SUN1 knockout experiments. 24 hours post-transfection cells were selected for expression of CRISPR-Cas9 with puromycin. Cells were allowed to recover and expand before selecting sequentially for antibiotic resistance gene expression. Cells surviving dual antibiotic selection (Blasticidin/Neomycin or Hygromycin-B/Zeocin) should contain double allele inserts. For initial SUN1 CRISPR experiment resulting in SUN1 knockdown a CRISPR-Cas9 construct was engineered to cut between amino acids 13 and 14 of SUN1. 550 bp HA's were designed immediately upstream and downstream of the cut site with a stop codon added to the 3' end of the 5' HA with insertion of either blasticidin or Neomycin resistance gene cassettes between the HA's. For the secondary SUN1 CRISPR experiment resulting in complete SUN1 knockout a CRISPR-Cas9 construct was engineered to cut 8 bp downstream of the second methionine codon. 550 bp HA's were designed immediately upstream and downstream of the 5' end of the second methionine codon (between amino acids 50 and 51) with two stop codons added to the 3' end of the 5' HA with either Hygromycin B or Zeocin resistance gene cassettes between the HA's. Following dual antibiotic selection serial dilutions were made to isolate single cell clonal lines. Whole cell lysates were made for Western blot analysis of SUN1 protein expression for each clonal line. Finally, immunofluorescent SUN1 labeling was performed on cell lines that were validated through Western blot analysis to confirm knockdown or knockout.

**4.3.5.6. SUN2 apple/GFP CRISPR.** SUN2 EGFP and mApple HDR CRISPR plasmids were created as follows: pUC19 vector (Thermo Scientific SD0061) was PCR amplified with a 5' primer located at the EcoRI site and a 3' primer located at the HindIII site in the MCS. 501 bp of 5' HA SUN2 genomic DNA directly upstream of the stop codon was PCR amplified with the addition of 5' pUC19 EcoRI homology (30 bp) and 3' homology (15 bp) to 5' EGFP/mApple sequence. EGFP/mApple was PCR amplified with the addition of 5' homology (15 bp) to the 3' end of SUN2 5' HA and 3' addition of a stop codon and homology (15 bp) to the 5' end of 3' HA SUN2. 501 bp of 3' HA SUN2 genomic DNA directly downstream and omitting the stop codon was PCR amplified with the addition of 5' homology (15 bp) to 3' EGFP/mApple sequence plus stop and 3' pUC19 HindIII homology (30 bp). PCR products were gel purified using QIAquick Gel Extraction Kit (Qiagen #28704). A Gibson reaction (Gibson et al., 2009) using a 1:1:1:1 M ratio was performed at 50 °C for 1 h. 3 µl of completed reaction was transformed into One Shot TOP10 chemically competent cells (Invitrogen C404003). DNA was extracted from cultured colonies using a QIAprep spin miniprep kit (Qiagen #27106). Correctly assembled pUC19-SUN2 EGFP/mApple HDR plasmids were verified through diagnostic digests and DNA sequencing. A CRISPR-Cas9 plasmid was engineered to cut 3 bp upstream of the SUN2 stop codon. CRISPR-Cas9 plasmid and pUC19-SUN2 EGFP/mApple HDR plasmids were transfected into WT MEF cells. 24 hours post-transfection cells were selected for expression of CRISPR-Cas9 with puromycin. Following selection, cells were expanded and then cells expressing SUN2 EGFP/mApple were isolated through FACS.

#### 4.3.6. Method details

**4.3.6.1. Western immunoblot analysis.** Cells were washed in PBS and lysed in RIPA buffer (150 mM NaCl, 0.5% NP-40, 0.1% SDS, 50 mM Tris-HCl pH 8.0, 0.1 M sodium fluoride, 0.2 mM sodium Ortho-vanadate) plus protease inhibitor cocktail (0.2 mM PMSF, 0.2 mM Benzamide HCl, 2 µg/ml Pepstatin A, 2 µg/ml Phenanthroline in ethanol) on ice. Cell debris was removed by centrifugation at 13,000 rpm for 10 min at 4 °C. Protein concentrations were measured (Bio-Rad DC Protein Assay Kit II #500-0112). Samples were boiled 3 min in SDS sample buffer (400 mM β-mercaptoethanol, 10% glycerol, 3% SDS, 62.5 mM Tris-HCl pH 6.8, bromophenol blue) and 10 or 30 µg/lane of protein was electrophoresed through 5% stacking/13% resolving SDS gel and transferred onto PVDF membranes in Tris/Glycine/Methanol buffer. Blots were blocked 1 h in 3% BSA/TBS-0.1% Tween at room temperature followed by washing 3 × 10 min in TBS-0.1% Tween. Blots were probed with SUN1 or vinculin antibodies 1 h at room temperature or overnight at 4 °C in 5% milk/TBS-0.1% Tween followed by washing 3 × 10 min in TBS-0.1% Tween at room temperature. Blots were probed 1 h at room temperature with HRP-conjugated secondary antibody (GE Healthcare NA931, 1:5000) and detected by ECL (GE Healthcare RPN2106).

**4.3.6.2. Uniaxial cyclic stretch for fixed immunofluorescent microscopy.** Cells were stretch stimulated using a custom-designed system previously described (Yoshigi et al., 2005). Briefly, cells were seeded onto precoated (25 µg/ml Collagen I and 2 µg/ml Fibronectin) silicone membranes (2.2 million cells onto three 26 × 33 mm membranes in a 10-cm plate) and grown to confluence overnight. Cells were subjected to uniaxial cyclic stretch (15%, 0.5 Hz, 1 h), then cells were fixed (3.7% formaldehyde 15 min) for cell staining and microscopy (Yoshigi et al., 2005; Hoffman et al., 2006).

**4.3.6.3. Uniaxial cyclic stretch for live cell fluorescent microscopy.** Stretching of live cells transfected with fluorescent proteins was performed on 15 B/C ratio (>1000 kPa) PDMS gels coupled to 20 nm FluoSpheres (Thermo Fisher F-8783), 25 µg/ml Collagen I (Fisher

Scientific CB-40236) and 2 µg/ml Fibronectin (Sigma F1141), mounted in ChamSlide imaging chamber (Quorum Technologies) in DMEM/F12, HEPES, no phenol red (Invitrogen #11039021) supplemented with 10% FBS, sodium pyruvate, L-glutamine, and penicillin/streptomycin (Gutierrez and Groisman, 2011). Stretch was applied using a condenser mounted indenter via a piezo controlled micropositioning stage. Stretch experiment were conducted as follows: homogeneous uniaxial stretch of ~5% strain was applied every 10 s with image capture every 60 s. Following each experiment an unstretched and stretched image of the gel was captured to verify the magnitude of the stretch.

**4.3.6.4. Microscopy.** Imaging of live unstretched and fixed stretched cells were performed on a Leica SP8 DMI8 inverted microscope with a Leica 63x Plan Achromatic 1.4 na oil objective (live) or Leica 40x Plan Achromatic 1.1 na water objective (fixed) using PMT and HyD detectors and LASX software (Leica). Image deconvolution was performed with Lightning software (Leica). Live cells were plated on fibronectin (5–10 µg/ml) coated coverslips and mounted in a magnetic ChamSlide imaging chamber in supplemented DMEM/F12 media. Stretched membranes were cut in quarters and quarter membranes were inverted on a ΔT dish (Bioprotechs) for imaging. Images were acquired at a depth of 8bit and 1024 × 1024 resolution. Z-stacks were acquired for each cell using the system-optimized step size. Live cells were imaged at 60 s intervals.

Live cell stretch imaging was performed on an Andor spinning disk confocal microscope. Illumination was provided by solid state 488, 568, and 647-nm lasers (Melles Griot). The lasers were switched by an acousto-optic tunable filter based laser combiner (Andor Technology). Illumination was delivered by optical fiber to the Yokogawa CSU-10 confocal scanhead. The emission light path was equipped with a dual bandpass filter (Semrock Inc.). The confocal system was mounted on an inverted Nikon TE300 microscope. Time-lapse image sequences were captured at a depth of 14bit using an Andor DV887 1024 × 1024 camera (Andor Technology) and a Nikon Apo TIRF 60 × 1.49 NA oil objective. Stage motions were controlled in XY with a Ludl XY stage (Ludl Electronic Products) and in Z with a Piezo stage insert (Mad City Labs). Image acquisition was performed using Andor IQ imaging software (Andor Technologies).

#### 4.4. Quantification and statistical analysis

##### 4.4.1. Model based analysis of fluorescent intensity

The quantification approaches in this paper rely on the identification of cellular organelles using software based surface modeling through Imaris (Bitplane). To identify the three dimensional positions of ALL lines and SFs, we used the Filaments feature which identifies linear objects as 'Filaments' in the image. The software uses an additional MATLAB Filament analysis plugin to break the Filament into 250 nm segments and then reports intensity statistics within these segments to allow fluorescent intensity measurements all along the length of the Filament. This enabled output to Excel (Microsoft) of mean intensity values for a given linear segment.

For quantification of the fluorescent intensity values for NPCs, we used the Spots feature in Imaris, which identifies and finds the center of, and reports various metrics and statistics of punctate objects. An additional MATLAB plugin for Imaris allows for the binning of Spots that are inside or outside a specified distance from a Filament.

##### 4.4.2. Statistical analysis

Mean intensity values for maximal intensity segments were graphed and subjected to t-tests in Prism (Graphpad). For Near-Far experiments, t-tests were performed as pairwise. Statistical significance is reported in the graphs ns = >0.05, 0.01–0.05 = \*, 0.001–0.01 = \*\*, 0.0001–0.001 = \*\*\*, 0.0001 = \*\*\*\*.

## Declarations

### Author contribution statement

Mark A. Smith and Elizabeth Blankman: Conceived and designed the experiments; Performed the experiments; Analyzed and interpreted the data; Wrote the paper.

Christopher C. Jensen: Performed the experiments.

Laura M. Hoffman, Katharine S. Ullman: Contributed reagents, materials, analysis tools or data.

Mary C. Beckerle: Conceived and designed the experiments.

### Funding statement

Mary C. Beckerle and Katharine S. Ullman were supported by National Institutes of Health General Medicine [R01-GM50877 & R01-GM131052].

### Data availability statement

Data will be made available on request.

### Declaration of interest's statement

The authors declare no competing interests.

### Additional information

Supplementary content related to this article has been published online at <https://doi.org/10.1016/j.heliyon.2022.e12147>.

### Acknowledgements

Thank you to the University of Utah Mutation Generation and Detection core for design and construction of CRISPR-Cas9 plasmids. Oligonucleotides were synthesized by the DNA/Peptide Facility, part of the Health Sciences Center Cores at the University of Utah. Sequencing was performed at the DNA sequencing Core Facility, University of Utah. We acknowledge Diana Lim for graphic design and figure preparation support. We acknowledge the Cell Imaging Core at the University of Utah for use of the Leica SP8 DMI8 inverted microscope. Research reported in this publication was supported by the Office of the Director of the National Institutes of Health under Award Number S10OD026959 also NCI Award Number 5P30CA042014-24.

### References

- Adams, R.L., Wente, S.R., 2013. Uncovering nuclear pore complexity with innovation. *Cell* 152, 1218–1221.
- Aragona, M., Panciera, T., Manfrin, A., Giullitti, S., Michielin, F., Elvassore, N., Dupont, S., Piccolo, S., 2013. A mechanical checkpoint controls multicellular growth through YAP/TAZ regulation by actin-processing factors. *Cell* 154, 1047–1059.
- Ateshian, G.A., Humphrey, J.D., 2012. Continuum mixture models of biological growth and remodeling: past successes and future opportunities. *Annu. Rev. Biomed. Eng.* 14, 97–111.
- Bindels, D.S., Haarbosch, L., Van Weeren, L., Postma, M., Wiese, K.E., Mastop, M., Aumonier, S., Gotthard, G., Royant, A., Hink, M.A., Gadella, T.W.J., 2017. mScarlet: a bright monomeric red fluorescent protein for cellular imaging. *Nat. Methods* 14, 53–56.
- Byers, H.R., White, G.E., Fujiwara, K., 1984. Organization and function of stress fibers in cells in vitro and in situ. A review. *Cell Muscle Motil.* 5, 83–137.
- Chang, W., Antoku, S., Ostlund, C., Worman, H.J., Gundersen, G.G., 2015. Linker of nucleoskeleton and cytoskeleton (LINC) complex-mediated actin-dependent nuclear positioning orients centrosomes in migrating myoblasts. *Nucleus* 6, 77–88.
- Cramer, L.P., Siebert, M., Mitchison, T.J., 1997. Identification of novel graded polarity actin filament bundles in locomoting heart fibroblasts: implications for the generation of motile force. *J. Cell Biol.* 136, 1287–1305.
- Crisp, M., Liu, Q., Roux, K., Rattner, J.B., Shanahan, C., Burke, B., Stahl, P.D., Hodzic, D., 2006. Coupling of the nucleus and cytoplasm: role of the LINC complex. *J. Cell Biol.* 172, 41–53.
- Deanfield, J.E., Halcox, J.P., Rabelink, T.J., 2007. Endothelial function and dysfunction. *Circulation* 115, 1285–1295.

- Driscoll, T.P., Cosgrove, B.D., Heo, S.J., Shurden, Z.E., Mauck, R.L., 2015. Cytoskeletal to nuclear strain transfer regulates YAP signaling in mesenchymal stem cells. *Biophys. J.* 108, 2783–2793.
- Dupont, S., Morsut, L., Aragona, M., Enzo, E., Giullitti, S., Cordenonsi, M., Zanconato, F., Le Digabel, J., Forcato, M., Bicciato, S., et al., 2011. Role of YAP/TAZ in mechanotransduction. *Nature* 474, 179–183.
- Elosegui-Artola, A., Andreu, I., Beedle, A.E.M., Lezamiz, A., Uroz, M., Kosmalska, A.J., Oria, R., Kechagia, J.Z., Rico-Lastres, P., Le Roux, A.L., et al., 2017. Force triggers YAP nuclear entry by regulating transport across nuclear pores. *Cell* 171, 1397–1410 e1314.
- Fournier, M.F., Sauser, R., Ambrosi, D., Meister, J.J., Verkhovsky, A.B., 2010. Force transmission in migrating cells. *J. Cell Biol.* 188, 287–297.
- Gibson, D.G., Young, L., Chuang, R.-Y., Venter, J.C., Hutchison, C.A., Smith, H.O., 2009. Enzymatic assembly of DNA molecules up to several hundred kilobases. *Nat. Methods* 6, 343–345.
- Gutierrez, E., Groisman, A., 2011. Measurements of elastic moduli of silicone gel substrates with a microfluidic device. *PLoS One* 6, e25534.
- Hennen, J., Saunders, C.A., Mueller, J.D., Luxton, G.W.G., 2018. Fluorescence fluctuation spectroscopy reveals differential SUN protein oligomerization in living cells. *Mol. Biol. Cell* 29, 1003–1011.
- Hoffman, L.M., Jensen, C.C., Kloeker, S., Wang, C.L., Yoshigi, M., Beckerle, M.C., 2006. Genetic ablation of zyxin causes Mena/VASP mislocalization, increased motility, and deficits in actin remodeling. *J. Cell Biol.* 172, 771–782.
- Hoffman, L.M., Smith, M.A., Jensen, C.C., Yoshigi, M., Blankman, E., Ullman, K.S., Beckerle, M.C., 2020. Mechanical stress triggers nuclear remodeling and the formation of transmembrane actin nuclear lines with associated nuclear pore complexes. *Mol. Biol. Cell* 31, 1774–1787.
- Hotulainen, P., Lappalainen, P., 2006. Stress fibers are generated by two distinct actin assembly mechanisms in motile cells. *J. Cell Biol.* 173, 383–394.
- Ingber, D.E., 1997. Tensegrity: the architectural basis of cellular mechanotransduction. *Annu. Rev. Physiol.* 59, 575–599.
- Jäckel, C., Nogueira, M.S., Ehni, N., Kraus, C., Ranke, J., Dohmann, M., Noessner, E., Nelson, P.J., 2016. A vector platform for the rapid and efficient engineering of stable complex transgenes. *Sci. Rep.* 6, 34365.
- Jahed, Z., Fadavi, D., Vu, U.T., Asgari, E., Luxton, G.W.G., Mofrad, M.R.K., 2018a. Molecular insights into the mechanisms of SUN1 oligomerization in the nuclear envelope. *Biophys. J.* 114, 1190–1203.
- Jahed, Z., Mofrad, M.R., 2019. The nucleus feels the force, LINCed in or not. *Curr. Opin. Cell Biol.* 58, 114–119.
- Jahed, Z., Soheilypour, M., Peyro, M., Mofrad, M.R.K., 2016. The LINC and NPC relationship – it's complicated. *J. Cell Sci.* 129, 3219–3229.
- Jahed, Z., Vu, U.T., Fadavi, D., Ke, H., Rathish, A., Kim, S.C.J., Feng, W., Mofrad, M.R.K., 2018b. A molecular model for LINC complex regulation: activation of SUN2 for KASH binding. *Mol. Biol. Cell* 29, 2012–2023.
- Jorgens, D.M., Inman, J.L., Wojcik, M., Robertson, C., Palsdottir, H., Tsai, W.-T., Huang, H., Bruni-Cardoso, A., López, C.S., Bissell, M.J., et al., 2016. Deep nuclear invaginations linked to cytoskeletal filaments: integrated bioimaging of epithelial cells in 3D culture. *J. Cell Sci.* 130, 177–189.
- Khatau, S.B., Kim, D.H., Hale, C.M., Bloom, R.J., Wirtz, D., 2010. The perinuclear actin cap in health and disease. *Nucleus* 1, 337–342.
- Kirby, T.J., Lammerding, J., 2018. Emerging views of the nucleus as a cellular mechanosensor. *Nat. Cell Biol.* 20, 373–381.
- Li, H., Beckman, K.A., Pessino, V., Huang, B., Weissman, J.S., Leonetti, M.D., 2017. Design and Specificity of Long ssDNA Donors for CRISPR-Based Knock-In. Cold Spring Harbor Laboratory.
- Li, P., Noegel, A.A., 2015. Inner Nuclear Envelope Protein SUN1 Plays a Prominent Role in Mammalian mRNA export. *Nucleic Acids Research* gkv1058.
- Li, Q., Kumar, A., Makhija, E., Shivashankar, G.V., 2014. The regulation of dynamic mechanical coupling between actin cytoskeleton and nucleus by matrix geometry. *Biomaterials* 35, 961–969.
- Liang, Y., Chiu, P.H., Yip, K.Y., Chan, S.Y., 2011. Subcellular localization of SUN2 is regulated by lamin A and Rab 5. *PLoS One* 6, e20507.
- Liu, Q., Pante, N., Misteli, T., Elsagga, M., Crisp, M., Hodzic, D., Burke, B., Roux, K.J., 2007. Functional association of Sun 1 with nuclear pore complexes. *J. Cell Biol.* 178, 785–798.
- Lombardi, M.L., Lammerding, J., 2011. Keeping the LINC: the importance of nucleocytoskeletal coupling in intracellular force transmission and cellular function. *Biochem. Soc. Trans.* 39, 1729–1734.
- Lu, W., Gotzmann, J., Sironi, L., Jaeger, V.M., Schneider, M., Luke, Y., Uhlen, M., Szgyarto, C.A., Brachner, A., Ellenberg, J., et al., 2008. Sun 1 forms immobile macromolecular assemblies at the nuclear envelope. *Biochim. Biophys. Acta* 1783, 2415–2426.
- Luxton, G.W., Gomes, E.R., Folker, E.S., Vintinner, E., Gundersen, G.G., 2010. Linear arrays of nuclear envelope proteins harness retrograde actin flow for nuclear movement. *Science* 329, 956–959.
- Luxton, G.W., Gomes, E.R., Folker, E.S., Worman, H.J., Gundersen, G.G., 2011. TAN lines: a novel nuclear envelope structure involved in nuclear positioning. *Nucleus* 2, 173–181.
- Maniotis, A.J., Bojanowski, K., Ingber, D.E., 1997a. Mechanical continuity and reversible chromosome disassembly within intact genomes removed from living cells. *J. Cell. Biochem.* 65, 114–130.
- Maniotis, A.J., Chen, C.S., Ingber, D.E., 1997b. Demonstration of mechanical connections between integrins, cytoskeletal filaments, and nucleoplasm that stabilize nuclear structure. *Proc. Natl. Acad. Sci. U. S. A.* 94, 849–854.
- Matsuda, T., Cepko, C.L., 2004. Electroporation and RNA interference in the rodent retina in vivo and in vitro. *Proc. Natl. Acad. Sci. USA* 101, 16–22.

- Mellad, J.A., Warren, D.T., Shanahan, C.M., 2011. Nesprins LINC the nucleus and cytoskeleton. *Curr. Opin. Cell Biol.* 23, 47–54.
- Naumanen, P., Lappalainen, P., Hotulainen, P., 2008. Mechanisms of actin stress fibre assembly. *J. Microsc.* 231, 446–454.
- Ostlund, C., Folker, E.S., Choi, J.C., Gomes, E.R., Gundersen, G.G., Worman, H.J., 2009. Dynamics and molecular interactions of linker of nucleoskeleton and cytoskeleton (LINC) complex proteins. *J. Cell Sci.* 122, 4099–4108.
- Rabut, G., Doye, V., Ellenberg, J., 2004. Mapping the dynamic organization of the nuclear pore complex inside single living cells. *Nat. Cell Biol.* 6, 1114–1121.
- Rajoo, S., Valloton, P., Onischenko, E., Weis, K., 2018. Stoichiometry and compositional plasticity of the yeast nuclear pore complex revealed by quantitative fluorescence microscopy. *Proc. Natl. Acad. Sci. U. S. A.* 115, E3969–E3977.
- Roshanzadeh, A., Nguyen, T.T., Nguyen, K.D., Kim, D.-S., Lee, B.-K., Lee, D.-W., Kim, E.-S., 2020. Mechanoadaptive organization of stress fiber subtypes in epithelial cells under cyclic stretches and stretch release. *Sci. Rep.* 10.
- Rosner, S.R., Pascoe, C.D., Blankman, E., Jensen, C.C., Krishnan, R., James, A.L., Elliot, J.G., Green, F.H., Liu, J.C., Seow, C.Y., et al., 2017. The actin regulator zyxin reinforces airway smooth muscle and accumulates in airways of fatal asthmatics. *PLoS One* 12, e0171728.
- Sabinina, V.J., Hossain, M.J., Hériché, J.-K., Hoess, P., Nijmeijer, B., Mosalaganti, S., Kueblbeck, M., Callegari, A., Szymborska, A., Beck, M., et al., 2021. Three-dimensional superresolution fluorescence microscopy maps the variable molecular architecture of the nuclear pore complex. *Mol. Biol. Cell* 32, 1523–1533.
- Schuller, A.P., Wojtynek, M., Mankus, D., Tatli, M., Kronenberg-Tenga, R., Regmi, S.G., Dip, P.V., Lytton-Jean, A.K.R., Brignole, E.J., Dasso, M., et al., 2021. The cellular environment shapes the nuclear pore complex architecture. *Nature* 598, 667–671.
- Smith, M.A., Blankman, E., Gardel, M.L., Luettjohann, L., Waterman, C.M., Beckerle, M.C., 2010. A zyxin-mediated mechanism for actin stress fiber maintenance and repair. *Dev. Cell* 19, 365–376.
- Starr, D.A., 2009. A nuclear-envelope bridge positions nuclei and moves chromosomes. *J. Cell Sci.* 122, 577–586.
- Starr, D.A., 2010. Cell biology. Nuclei get TAN lines. *Science* 329, 909–910.
- Starr, D.A., Fridolfsson, H.N., 2010. Interactions between nuclei and the cytoskeleton are mediated by SUN-KASH nuclear-envelope bridges. *Annu. Rev. Cell Dev. Biol.* 26, 421–444.
- Stewart-Hutchinson, P.J., Hale, C.M., Wirtz, D., Hodzic, D., 2008. Structural requirements for the assembly of LINC complexes and their function in cellular mechanical stiffness. *Exp. Cell Res.* 314, 1892–1905.
- Supharattanasitthi, W., Carlsson, E., Sharif, U., Paraoan, L., 2019. CRISPR/Cas9-mediated one step bi-allelic change of genomic DNA in iPSCs and human RPE cells in vitro with dual antibiotic selection. *Sci. Rep.* 9.
- Talamas, J.A., Hetzer, M.W., 2011. POM121 and Sun 1 play a role in early steps of interphase NPC assembly. *J. Cell Biol.* 194, 27–37.
- Versaevael, M., Braquenier, J.B., Riaz, M., Grevesse, T., Lantoine, J., Gabriele, S., 2014. Super-resolution microscopy reveals LINC complex recruitment at nuclear indentation sites. *Sci. Rep.* 4, 7362.
- Wong, A.J., Pollard, T.D., Herman, I.M., 1983. Actin filament stress fibers in vascular endothelial cells in vivo. *Science* 219, 867–869.
- Yoshigi, M., Hoffman, L.M., Jensen, C.C., Yost, H.J., Beckerle, M.C., 2005. Mechanical force mobilizes zyxin from focal adhesions to actin filaments and regulates cytoskeletal reinforcement. *J. Cell Biol.* 171, 209–215.
- Zimmerli, C.E., Allegretti, M., Rantos, V., Goetz, S.K., Obarska-Kosinska, A., Zagoriy, I., Halavatyi, A., Hummer, G., Mahamid, J., Kosinski, J., Beck, M., 2021. Nuclear pores dilate and constrict in cellulose. *Science* 374.